The Astrophysical Journal, 984:20 (17pp), 2025 May 1 https://doi.org/10.3847/1538-4357/adc110

Warm Ionized Gas Outflows in Active Galactic Nuclei: What Causes Them?

Payel Nandi[1,2], C. S. Stalin[1], and D. J. Saikia[3]
[1] Indian Institute of Astrophysics, Block II, Koramangala, Bangalore, 560034, India; payel.nandi@iiap.res.in
[2] Joint Astronomy Programme, Department of Physics, Indian Institute of Science, Bangalore, 560012, India
[3] Inter-University Centre for Astronomy and Astrophysics, IUCAA, Pune, 411007, India
Received 2024 October 27; revised 2025 February 18; accepted 2025 March 9; published 2025 April 22

Abstract

The driving force behind outflows, often invoked to understand the correlation between the supermassive black holes powering active galactic nuclei (AGN) and their host galaxy properties, remains uncertain. We provide new insights into the mechanisms that trigger warm ionized outflows in AGN, based on findings from the MaNGA survey. Our sample comprises 538 AGN with strong [O III] λ5007 emission lines, of which 197 are detected in radio and 341 are radio-undetected. We analyzed the [O III] λ5007 line in summed spectra, extracted over their central $500 \times 500\ \mathrm{pc}^2$ region. The calculated Balmer 4000 Å break, D_n4000, is larger than 1.45 for ∼95% of the sources, indicating that the specific star formation rate in their central regions is less than $10^{-11.5}\ \mathrm{yr}^{-1}$, which points to evidence of negative AGN feedback suppressing star formation. Considering the whole sample, radio-detected sources show a greater outflow detection rate (56% ± 7%) than radio-undetected sources (25% ± 3%). They also show higher velocity, mass outflow rate, outflow power, and outflow momentum rate. We noticed a strong correlation between outflow characteristics and bolometric luminosity in both samples, except that the correlation is steeper for the radio-detected sample. Our findings suggest that (a) warm ionized outflows are prevalent in all types of AGN, (b) radiation from AGN is the primary driver of these outflows, (c) radio jets are likely to play a secondary role in enhancing the gas kinematics over and above that caused by radiation, and (d) there is very little star formation in the central regions of the galaxies, possibly due to negative feedback from AGN activity.

Unified Astronomy Thesaurus concepts: AGN host galaxies (2017); Active galaxies (17); Seyfert galaxies (1447); LINER galaxies (925); Radio jets (1347)

1. Introduction

Supermassive black holes (SMBHs) with masses (M_{BH}) greater than $10^6\ M_\odot$ are generally known to reside at the centers of all massive galaxies in the Universe (I. Martín-Navarro et al. 2018 and references therein). A small fraction of these galaxies host active galactic nuclei (AGN) caused by the accretion of matter from the surroundings by these SMBHs (P. Padovani et al. 2017), though they are less common in dwarf galaxies that host intermediate-mass black holes with $M_{\mathrm{BH}} < 10^6\ M_\odot$ (A. E. Reines 2022). The process of accretion, which leads to the release of enormous amounts of energy in the form of radiation (D. Lynden-Bell 1969) as well as particles via relativistic jets (A. Cattaneo & P. N. Best 2009), is believed to affect their host galaxies via a process called feedback. AGN feedback is invoked to explain the observed correlation between M_{BH} and various host galaxy properties (M.-Y. Zhuang & L. C. Ho 2023 and references therein).

A viable feedback mechanism in AGN is outflows. These outflows are dynamic phenomena, representing the expulsion of vast amounts of matter and energy from the vicinity of SMBHs at the centers of galaxies. They play a crucial role in shaping the surrounding environment and influencing the evolution of galaxies (Y. Guo et al. 2023). They are multifaceted, as seen in molecular, neutral, and ionized gas (T. Izumi et al. 2023; P. Nandi et al. 2023b; R. A. Riffel et al. 2023; R. Su et al. 2023), and can occur on various scales, spanning from relatively small-scale winds to colossal jets extending over intergalactic distances (C. M. Harrison et al. 2014; D. J. Saikia 2022; T. Izumi et al. 2023; Y. Guo et al. 2023; P. Nandi et al. 2023b, for a review). They can profoundly impact the galaxy's evolution by regulating the rate of star formation, distributing elements crucial for planetary systems, and even influencing the growth of SMBHs (P. Nandi et al. 2023a; G. Venturi et al. 2023; P. Nandi et al. 2024). Irrespective of outflows being prevalent in AGN, answers to questions such as (a) what drives these outflows and (b) at what scales they operate are not conclusively known and are highly debated. The potential mechanisms that could drive these outflows could be radiation and/or radio jets (D. Wylezalek & R. Morganti 2018).

Studies are available in the literature aimed at identifying the main driving mechanisms of outflows. They are focused on individual systems as well as on a sample of sources. For example, the correlation noticed between the ionized [O III] λ5007 gas outflow and the radio jet in NGC 1068 seems to favor a jet-driven outflow (S. García-Burillo et al. 2014; G. Venturi et al. 2021). In IC 5063, R. Morganti et al. (2015) found evidence of molecular, atomic, and ionized outflows and conclude that both the radiation and jet could drive the outflow, but with the jet being the dominant driver. Other studies that find in favor of jets triggering outflows include that of NGC 1337 (S. Aalto et al. 2016), a sample of 10 quasars at $z < 0.2$ (M. E. Jarvis et al. 2019), 3C 273 (B. Husemann et al. 2019), ESO 420−G13 (J. A. Fernández-Ontiveros et al. 2020), NGC 5643 (G. Venturi et al. 2021), NGC 1386 (G. Venturi et al. 2021), J1316+1753 (A. Girdhar et al. 2022), B2 0258 +35 (S. Murthy et al. 2022), N0945+1737 (G. Speranza et al. 2022), the Teacup galaxy (A. Audibert et al. 2023), and the dwarf AGN NGC 4395 (P. Nandi et al. 2023b). However, observations of Mrk 231 support radiation from accretion

driving the outflow (C. Feruglio et al. 2015). While the above studies are focused on using high-resolution observations, studies at low spatial resolution do exist. J. R. Mullaney et al. (2013) analysed a larger sample of quasars using the Sloan Digital Sky Survey (SDSS)[4] spectra and found that sources more luminous in the radio band tend to have a broader [O III] λ5007 line profile, while N. L. Zakamska & J. E. Greene (2014) found in favor of outflows being driven via radiative output from quasars. From an analysis of SDSS spectra of Type 2 AGN, J.-H. Woo et al. (2016) found that while outflows are prevalent in Type 2 AGN, they are not directly related to radio activity. Alternatively, from an analysis of the SDSS spectra of radio AGN, P. Kukreti et al. (2023) found that radio jets are more effective in driving outflows when they are young. S. J. Molyneux et al. (2019) also found that the chance of finding outflows is greater in compact radio sources that possibly host young radio jets. Recently, from an analysis of a large sample of AGN, M. Liao et al. (2024) found the outflow velocity to correlate with radio power. However, A. Ayubinia et al. (2023) conclude that both accretion and radio activity can have a role in driving outflows.

These studies aimed at finding the driver of outflows have focused on both radio-loud and radio-quiet quasars. This is misleading as even radio-quiet quasars are found to have radio jets that could impact the outflow. Also, the separation of quasars into radio-loud and radio-quiet is questioned, and an alternative division of AGN into jetted and nonjetted sources is proposed (P. Padovani 2017). Thus, the driver for outflows in AGN remains unsettled. To overcome the above limitations, first, we utilized in this work a sample of AGN separated into radio-detected and radio-undetected. This inclusion of radio-undetected sources makes sure that these sources lack clear signatures of radio jets (considering that the radio emission in radio-detected AGN is due to jets in them and not due to star formation in their hosts) at the sensitivity levels of existing radio surveys. And, second, we used spatially resolved spectroscopic data on a large sample of AGN hitherto not utilized for such a comparative study.

2. Sample

Our initial sample of sources was derived from the Mapping Nearby Galaxies at Apache Point Observatory (MaNGA; K. Bundy et al. 2015) survey, a spectroscopic program under SDSS-IV. MaNGA employs a fiber-based integral field unit (IFU) spectroscopic technique, utilizing the two BOSS spectrographs mounted on the 2.5 m Sloan Foundation Telescope at Apache Point Observatory. MaNGA has observed 10,010 unique galaxies with redshifts ranging from 0.01 to 0.15 (D. A. Wake et al. 2017), using different IFU configurations. The spatial resolution achieved is between $2''$ and $2.''5$, with a spectral resolution of approximately 2000. The program's field of view varies from $12''$ to $32''$, depending on the IFU configuration, and covers a spatial range of 1.5–2.5 effective radii of the observed galaxies. We cross-correlated the sources in the MaNGA catalog (D. A. Wake et al. 2017) with the latest version of the Million Quasars Catalogue (MILLIQUAS; E. W. Flesch 2023) to identify genuine AGN in the MaNGA catalog, using a search radius of $2''$. MILLIQUAS is a collection of all published AGN and quasars until 2023 June 30, amounting to a total of 1,021,800 sources. Our cross-correlation of MaNGA sources with MILLIQUAS led to a sample of 1142 AGN. As these sources were pulled from various surveys in MILLIQUAS, we checked the position of these 1142 sources in the Baldwin–Phillips–Terlevich (BPT) diagram (J. A. Baldwin et al. 1981) for homogeneity. We took an aperture of a 500 pc $\times$ 500 pc square box centered on the source and calculated the flux values of the [O III] λ5007, Hβ, Hα, [N II] λ6584, [S II] λ6718, and [S II] λ6732 lines from the Data Analysis Pipeline (DAP) products (K. B. Westfall et al. 2019) of MaNGA. Then, we plotted the flux ratio between [O III] λ5007 and Hβ against that between [S II] λ(6717+6732) and Hα, and also the flux ratio between [O III] λ5007 and Hβ against that between [N II] λ6584 and Hα for the sources in the BPT diagrams. Then, out of these 1142 sources, 718 are above the star formation line in the [S II] λ(6717 +6732)/Hα versus [O III] λ5007/Hβ diagram and 740 sources lie above the star formation line in the [N II]λ6584/Hα versus [O III]λ5007/Hβ diagram, with 688 common sources in both the BPT diagrams. We considered these 688 AGN for our analysis, of which 252 are Seyferts and 436 are LINERs.

We cross-matched these 688 AGN with the Very Large Array (VLA) Faint Images of the Radio Sky at Twenty Centimeters (FIRST) survey (R. H. Becker et al. 1995) using an angular separation of $3''$. The FIRST survey, conducted with the NRAO VLA in its B-configuration, provides radio maps of the sky at 20 cm (1.4 GHz) with a beam size of approximately $5.''4$ and a typical rms noise level of 0.14 mJy beam^{-1}. Through this cross-matching process, we identified 217 AGN with radio counterparts in the FIRST catalog that exhibiting flux densities greater than 0.5 mJy, classifying them as radio-detected. The remaining 471 AGN, lacking radio counterparts in the FIRST survey, were categorized as radio-undetected. Out of these 471 sources, 18 sources are not covered by the FIRST survey. Neglecting those 18 sources, our final radio-undetected sample consists of 453 sources. Of the 217 radio-detected sample, 95 sources are Seyfert-type AGN while 122 are LINERs. Similarly, among the 453 radio-undetected sample, 149 sources are Seyfert-type AGN while 304 sources are LINERs. The positions of these sources in the BPT diagrams are shown in Appendix A (see Figure A1). The radio-detected and the radio-undetected samples have similar distributions in the redshift and optical *B*-band brightness plane (see Figure A2). A Kolmogorov–Smirnov (KS) test carried out on their distributions of redshift and *B*-band brightness indicates that the two samples are indeed indistinguishable with statistics of 0.07 and a *p*-value of 0.12.

3. Analysis

We focused our analysis on a total of 217 AGN with radio detection and 453 AGN without radio detection in the FIRST survey. For this, we used the data reduction pipeline (DRP) products (D. R. Law et al. 2016) LOGCUBE of SDSS DR17. The DRP products contain the processed and calibrated spectra for each spaxel in the field of view in form of a cube for each source.

For each of the sources studied in this work, we generated summed spectra in the rest frame of the sources over a square with sides of length 500 pc. The choice of 500 pc is due to our requirement of having at least one spaxel to generate the spectra for most of the sources.

We fitted the [O III] λ5007 profile with multiple Gaussian components along with a first-order polynomial for the continuum using the nonlinear least-squares fitting algorithm within the *curvefit* module in the *Scipy* library. We fitted [O III]

[4] https://sdss.org/

Table 1
Summary of the Sources Analysed for Ionized Outflows in the [O III] λ5007 Line

	Total Sample		Radio-detected			Radio-undetected		
	Seyferts	LINERs	Total	Seyferts	LINERs	Total	Seyferts	LINERs
Total number of sources	223	315	197	92	105	341	131	210
Number of source with one Gaussian component	76	267	86	11	75	257	65	192
Number of sources with two Gaussian components	99	47	77	47	30	69	52	17
Number of sources with three Gaussian components	48	1	34	34	0	15	14	1
Number of sources with outflow	147	48	111	81	30	84	66	18
Outflow detection rate as a percentage	66 ± 7	15 ± 2	56 ± 7	88 ± 13	29 ± 6	25 ± 3	50 ± 8	8 ± 2

λ5007 because we are only interested in the warm ionized phase of outflow, which is traced by the forbidden bright line [O III] λ5007. During the fit, we kept the width, peak, and amplitude of each of the components as free parameters. Also, we restricted the fitting to those sources for which the signal-to-noise ratio (SNR) of the line is more than 3.0. Here, SNR refers to the ratio of the flux at the peak of the line to the standard deviation of continuum fluxes on either side of the line. We used a total width of 80 Å for the spectral region (4977–5057 Å) during the fitting. For some sources, the [O III] λ5007 line profile was adequately modeled with a single Gaussian component. However, in cases where the residual, defined as (data – model)/data, exceeded 10%, additional Gaussian components were considered. The residual was reassessed after each addition and compared to the previous fit. If including an additional Gaussian reduced the residual and smoothed fluctuations in both the surrounding continuum and the line region, the extra component was adopted. Otherwise, the fit was restricted to the minimum number of Gaussian components required. For cases where more than one Gaussian component was necessary, an additional criterion was applied: the peaks of the second and third components have to exceed three times the standard deviation of the continuum fluxes to confirm their statistical significance. In the radio-detected sample, the SNR of the first outflow component ranges from 10 to 306, while the SNR of the second outflow component ranges from 8 to 331. In the radio-undetected sample, the SNR of the first outflow component ranges from 4 to 199, and the SNR of the second ranges from 3 to 122. We show in Figure A3 the spectral fits to three sources, one requiring a single Gaussian component and the others requiring two and three Gaussian components, respectively. We also manually inspected each of the fitted spectra to ensure their fitting was correct.

After the fitting, we corrected the measured outflow fluxes for Galactic extinction using J. A. Cardelli et al. (1989) and the $E(B-V)$ values given in the header of DRP files. The fluxes were also corrected for internal extinction using the Hα/Hβ ratio taken from DAP products and following J. S. Miller & W. G. Mathews (1972), S. Veilleux et al. (1995), and D. Calzetti et al. (2000). Under the theoretical assumption of case B recombination, the intrinsic Hα/Hβ ratio was taken as 3.1 (D. E. Osterbrock & G. J. Ferland 2006).

4. Results and Discussion

4.1. Detection of Outflows

For both the radio-detected and the radio-undetected samples, we searched for the signature of outflows over a region of 500×500 pc^2 centered on each of the sources. The [O III] λ5007 line was detected at the 3σ limit for 197 sources in the radio-detected category and 341 sources in the radio-undetected category. Our final sample thus consists of a total of 538 sources with strong [O III] λ5007 for further analysis.

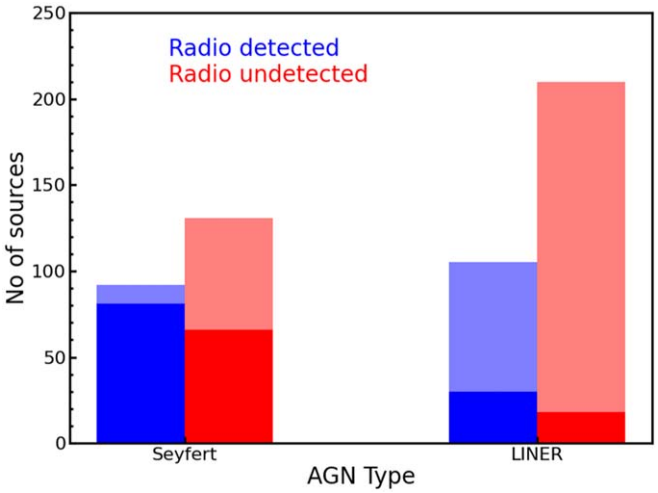

Figure 1. Bar chart of the different types of AGN (Seyferts and LINERs) used in this study. Here, the large blue bar refers to the total radio-detected sources, and the large red bar refers to the total radio-undetected sources. Dark-shaded regions refer to outflow-detected sources.

In the radio-detected sample, for 86 out of 197 sources, a single Gaussian component proved sufficient for fitting the [O III] λ5007 line; for 77 sources, two Gaussian components were needed to fit the line, while for 34 sources three Gaussian components were needed. Considering sources that require more than one Gaussian component to represent the [O III] λ5007 line well, in the radio-detected category, a total of 111 out of 197 sources ($56\% \pm 7\%$) prominently showed discernible signatures indicative of outflows.

Similarly, in the radio-undetected sample, 257 out of the 341 sources required a single Gaussian component to represent the [O III] λ5007 line well, while 69 sources required two Gaussian components and 15 sources needed three. Thus, in the radio-undetected sample, we detected outflows for 84 sources, i.e., $25\% \pm 3\%$ of the sources showed signatures of outflows. This clearly indicates that the outflow detection rate is higher in the radio-detected sample than in the radio-undetected sample.

We also classified our sample into Seyferts and LINERs based on their location in the BPT diagram (Figure A1) to investigate their prevalence of outflows. In the radio-detected sample, we have 92 Seyferts and 105 LINERs for which [O III] λ5007 was significantly detected. Of these, we detected outflows in 81 Seyferts and 30 LINERs. Similarly, in the radio-undetected sample, we detected the [O III] λ5007 line in 131 Seyferts and 210 LINERs. Of these, we detected outflows in 66 Seyferts and 18 LINERs. The results of the analysis are summarized in Table 1 and in Figure 1.

Table 2
Kinematic Properties of the Brightest Outflows

(a) Radio-detected

Parameter	Total			Seyferts			LINERs		
	Range	Mean	Median	Range	Mean	Median	Range	Mean	Median
V_{shift} (km s^{-1})	−782 to 463	−178	−163	−782 to 463	−106	−89	−695 to 258	−376	−449
FWHM$_{out}$ (km s^{-1})	169–1398	646	626	169–1398	635	611	257–1018	678	737
V_{out} (km s^{-1})	271–1970	788	705	271–1970	720	642	378–1400	973	1084.0
AI	−0.46 to 0.12	−0.15	−0.16	−0.34 to 0.12	−0.14	−0.15	−0.46 to 0.11	−0.18	−0.16
M_{out} (10^2 $M_\odot$)	1.81–23,681.85	1069.71	348.47	1.89–23,681.85	1362.98	507.71	1.81–2120.98	273.70	41.16
$\dot{M}_{out}$ (10^{-3} $M_\odot$ yr^{-1})	0.23–5112.32	166.56	43.28	0.23–5112.32	212.13	59.45	0.33–424.39	42.87	8.02
KP$_{out}$ (10^{38} erg s^{-1})	0.20– 18,166.25	461.92	48.25	0.24–18,166.25	591.12	55.63	0.20–1425.12	111.26	34.40
$\dot{P}_{out}$ (10^{30} g cm s^{-2})	0.83–34,222.09	923.43	165.39	0.83–34,222.09	1177.20	198.87	0.91–2761.69	234.64	60.19

(b) Radio-undetected

Parameter	Total			Seyferts			LINERs		
	Range	Mean	Median	Range	Mean	Median	Range	Mean	Median
V_{shift} (km s^{-1})	−628 to 108	−234	−167	−628 to 108	−173	−134	−624 to −211	−526	−585
FWHM$_{out}$ (km s^{-1})	140–1171	526	518	140–865	485	443	580–1171	720	672
V_{out} (km s^{-1})	118–1387	691	610	188–1274	598	487	849–1387	1137	1136
AI	−0.51 to 0.16	−0.18	−0.17	−0.51 to 0.16	−0.15	−0.13	−0.44 to −0.01	−0.33	−0.37
M_{out} (10^2 $M_\odot$)	0.30–1488.24	252.60	96.10	4.70–1488.25	288.80	114.74	0.30–616.59	79.95	33.35
$\dot{M}_{out}$ (10^{-3} $M_\odot$ yr^{-1})	0.080–173.53	26.34	11.34	0.95–173.53	27.85	12.61	0.08–151.93	19.11	7.42
KP$_{out}$ (10^{38} erg s^{-1})	0.33–696.00	42.20	12.92	0.33–296.34	33.46	12.88	0.36–696.00	83.90	22.41
$\dot{P}_{out}$ (10^{30} g cm s^{-2})	0.58–1154.74	106.05	50.95	1.99–793.52	98.54	49.45	0.58–1154.74	141.85	50.95

Considering the total sample, we found that $66\% \pm 7\%$ of Seyferts show outflows, compared to only $15\% \pm 2\%$ of LINERs. In radio-detected Seyferts, outflows are detected in $88\% \pm 13\%$ sources, while in radio-detected LINERs, it is $29\% \pm 6\%$. In the case of the radio-undetected sample, we detected outflows for $50\% \pm 8\%$ Seyferts and $8\% \pm 2\%$ LINERs. Thus Seyferts consistently show outflows more frequently than LINERs, both in radio-detected and radio-undetected samples. This is in agreement with a recent study by J. P. Torres-Papaqui et al. (2024), who also made a systematic analysis of the SDSS spectra of a large sample of Seyferts and LINERs and found that the probability of detecting outflows is lower in LINERs than in Seyferts.

4.2. Comparison of Kinematic Properties of Outflow

In the following sections, we compare the kinematic properties of outflows in our sample of sources. In cases where two outflowing components were detected, we initially consider only the brighter of the two in the analysis of the kinematic properties of the outflow. We later also consider the outflowing component of lower brightness, and also the one with the higher velocity. The values for the brighter component are tabulated in Table 2 for the total sample, the Seyferts, and the LINERs, and among them separately into radio-detected and radio-undetected samples. Similar tables for the other two cases are given in Appendix B.

4.2.1. Velocity Shift

We measured the velocity shift (V_{shift}) of the outflowing component relative to the narrow component of the [O III] λ5007 emission line. In this definition, a negative value of V_{shift} corresponds to the broad blueshifted component and a positive value of V_{shift} corresponds to the broad redshifted component. The distribution of V_{shift} for both the radio-detected and radio-undetected samples of sources is shown in the upper left panel of Figure 2. The KS test reveals that the distributions of the two samples are not statistically different, with a p-value of 0.4. For the radio-detected sample, V_{shift} ranges from $-782\,km\,s^{-1}$ to $463\,km\,s^{-1}$, with a mean of $-178\,km\,s^{-1}$ and a median of $-163\,km\,s^{-1}$ with median uncertainty of $46\,km\,s^{-1}$. Similarly for the radio-undetected sample, V_{shift} ranges from $-628\,km\,s^{-1}$ to $108\,km\,s^{-1}$, with a mean of $-234\,km\,s^{-1}$ and a median of $-167\,km\,s^{-1}$ with median uncertainty of $70\,km\,s^{-1}$. In both our samples, we found more sources ($\sim$80%) to show blue asymmetries of their [O III] λ5007 line than red asymmetry. This could be because of the redshifted part of the bipolar outflow being obscured by dust and/or seen at a lower S/N than the blueshifted component and thus being undetected (S. Belli et al. 2024).

4.2.2. Velocity Dispersion

We parameterize the emission line profile of the outflowing component using the dispersion of the line parameter ($\sigma_{measured}$) obtained from the fitting of the [O III] λ5007 line. This measured velocity dispersion of the outflowing component, $\sigma^2_{measured} = \sigma^2_{out} + \sigma^2_{inst}$, where σ_{out} and σ_{inst} are the intrinsic velocity dispersion of the outflowing component and the dispersion of the instrumental line-spread function. For MaNGA, the 1σ width of the instrumental line-spread function is $\sim 70\,km\,s^{-1}$ (D. R. Law et al. 2022). To estimate σ_{out}, we subtracted σ_{inst} from $\sigma_{measured}$ in quadrature. From the estimated σ_{out}, we calculated the FWHM of the outflowing component as $FWHM_{out} = 2\sqrt{2\ln 2}\,\sigma_{out} = 2.35\sigma_{out}$, which is valid for a true Gaussian profile. The distribution of FWHM$_{out}$ is shown in the upper middle panel of Figure 2 for both the radio-detected and radio-undetected samples.

For the radio-detected category, FWHM$_{out}$ ranges from $169\,km\,s^{-1}$ to $1398\,km\,s^{-1}$, with a mean value of $646\,km\,s^{-1}$ and a median of $626\,km\,s^{-1}$ with median uncertainty of

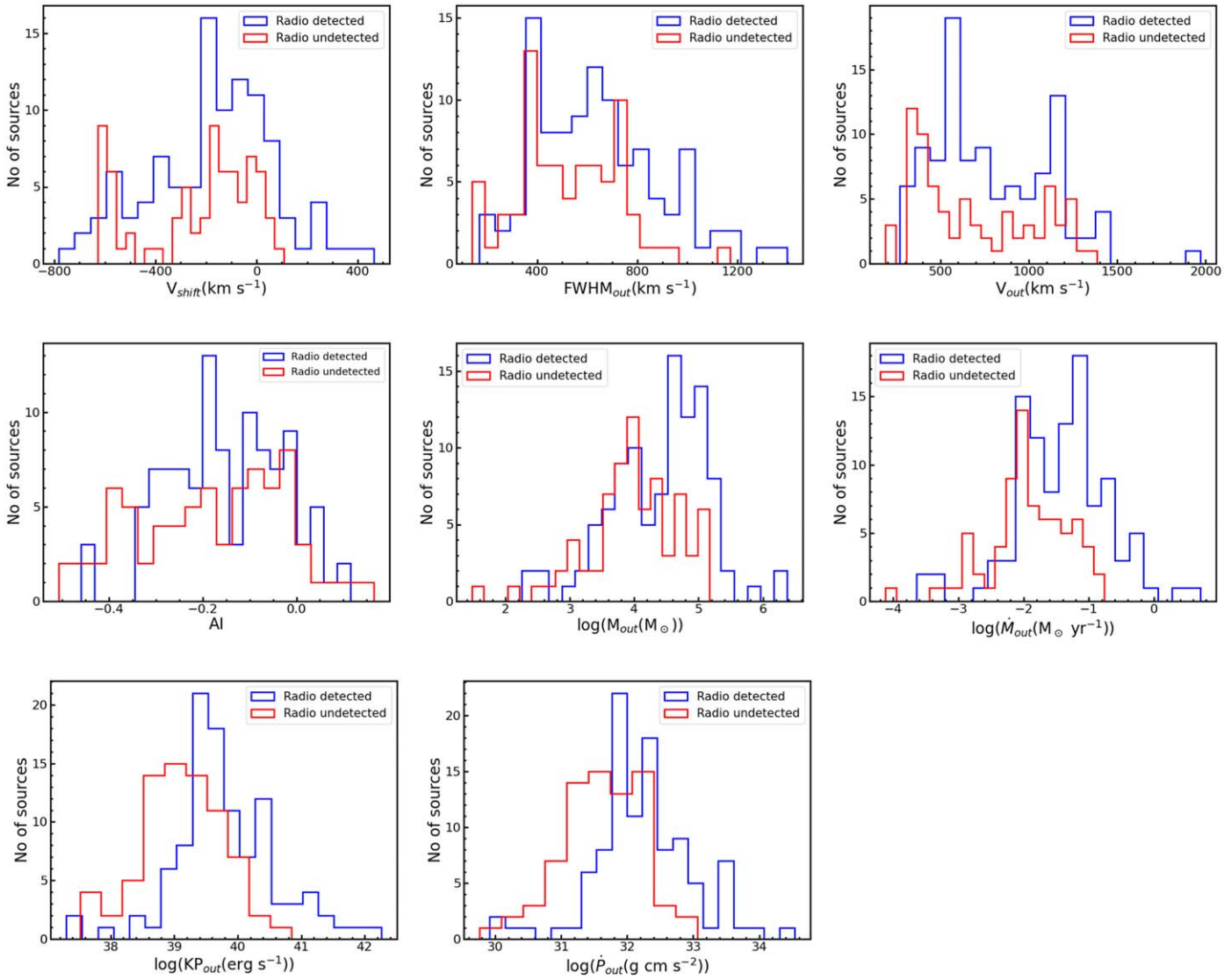

Figure 2. Histograms of different kinematic properties of outflows. The parameters are labeled in the respective plots. The blue and red histograms are for the radio-detected and radio-undetected samples, respectively.

59 km s^{-1}. For the radio-undetected category, FWHM$_{out}$ ranges from 140 km s^{-1} to 1171 km s^{-1} and it is lower than for the radio-detected sample, with a mean of 526 km s^{-1} and a median of 518 km s^{-1} along with median uncertainty of 82 km s^{-1}. Therefore, this larger range and the higher values of FWHM$_{out}$ for radio-detected sources indicate that the outflowing material in them is more kinematically disturbed than in radio-undetected sources.

4.2.3. Outflow Velocity

We define the outflow velocity, V_{out}, as the sum of the velocity difference ($|V_{shift}|$) between the outflowing component and the narrow component plus two times the standard deviation of the outflowing component (σ_{out}), i.e., $V_{out} = |V_{shift}| + 2\sigma_{out}$ (E. Parlanti et al. 2024). The distribution of V_{out} is shown in the upper right panel of Figure 2 for both the radio-detected and radio-undetected samples. The KS test indicates that the distributions of the radio-detected and radio-undetected populations are statistically distinct, with a p-value of 6×10^{-3}. This low p-value suggests that the likelihood of these two distributions being drawn from the same parent population is very low.

For the radio-detected sample, the outflow velocity V_{out} spans from 271 km s^{-1} to 1970 km s^{-1}, with an average velocity of 788 km s^{-1} and a median velocity of 705 km s^{-1} with median uncertainty of 74 km s^{-1}. In contrast, the radio-undetected sources exhibit a range of V_{out} from 118 km s^{-1} to 1387 km s^{-1}, with a lower mean velocity of 691 km s^{-1} and a median of 610 km s^{-1} along with median uncertainty of 98 km s^{-1}. The higher velocities in the radio-detected sample may imply that radio emission is linked to more powerful or sustained outflows, possibly associated with jet-driven mechanisms or enhanced AGN activity. The contrast in median and mean velocities between the two samples supports the idea of a significant difference in outflow dynamics related to the presence of radio emission.

4.2.4. Asymmetric Index

To evaluate the asymmetry of the total [O III] λ5007 line profile, we utilize the asymmetry index (AI). Following

N. L. Zakamska & J. E. Greene (2014), the AI is defined as

$$\mathrm{AI} = \frac{(\mathrm{V95} - \mathrm{V50}) - (\mathrm{V50} - \mathrm{V05})}{\mathrm{V95} - \mathrm{V05}} \quad (1)$$

Here V95, V50, and V05 are the velocities at which 95%, 50%, and 5% of the emission line flux is found. A value of zero indicates a symmetric profile, a positive value suggests redshifted wings, and a negative value indicates blueshifted wings. The middle left panel of Figure 2 displays the distribution of AI values for both the radio-detected and radio-undetected samples. Statistically, these distributions differ, with a KS test statistic of 0.32 and a p-value of 0.04, suggesting a significant but moderate distinction between the two groups.

For the radio-detected sample, AI values range from −0.46 to 0.12, with an average of −0.15 and a median of −0.16 with median uncertainty of 0.05. In contrast, the radio-undetected sample has a wider range from −0.51 to 0.16, with a mean value of −0.18 and a median of −0.17 with median uncertainty of 0.10. The consistently negative AI in both the samples suggests the dominance of the blueshifted component of the bipolar outflow over its redshifted component, as discussed in Section 4.2.1.

4.2.5. Outflow Mass

We determined the mass of the outflowing gas ($M_{\rm out}$) following S. Carniani et al. (2024) as

$$M_{\rm out} = 0.8 \times 10^8 \left(\frac{L_{[\rm O\,III]out}}{10^{44}\ \rm erg\ s^{-1}}\right)\left(\frac{500\ \rm cm^{-3}}{n_e}\right)\left(\frac{Z_\odot}{Z}\right) M_\odot. \quad (2)$$

Here, $L_{[\rm O\,III]out}$ is the luminosity of the outflowing component calculated from the flux of the outflowing component of [O III] λ5007 and corrected for dust extinction following the procedure given in Section 3. The outflow mass also depends on both the electron density (n_e) and the gas-phase metallicity of the medium. We calculated n_e using the ratio of [S II] λ6718 to [S II] λ6732, assuming an electron temperature of 10,000 K, using *pyneb* (V. Luridiana et al. 2015). We also determined the gas-phase metallicity using [O III] $\lambda\lambda$4959, 5007, [N II] $\lambda\lambda$6548, 6584, and the Balmer lines (Hα and Hβ), as described by J. C. do Nascimento et al. (2022).

The distribution of $M_{\rm out}$ for both the radio-detected and radio-undetected samples is illustrated in the middle panel of Figure 2. A KS test shows that the two distributions are statistically distinct, with a p-value of 6×10^{-4}. For the radio-detected sample, $M_{\rm out}$ ranges from 181 $M_\odot$ to 2.4×10^6 $M_\odot$, with a mean of 1.1×10^5 $M_\odot$ and a median of 3.5×10^4 $M_\odot$ with median uncertainty of 1.4×10^3 $M_\odot$. In contrast, the radio-undetected sample shows $M_{\rm out}$ values ranging from 30 $M_\odot$ to 1.5×10^5 $M_\odot$, with a mean of 2.5×10^4 $M_\odot$ and a median of 9.6×10^3 $M_\odot$ along with median uncertainty of 8.6×10^2 $M_\odot$. This finding suggests that outflow masses are notably higher in radio-detected sources than in radio-undetected sources.

4.2.6. Mass Outflow Rate

We calculated the mass outflow rate ($\dot{M}_{\rm out}$), which represents the mass of gas outflowing per unit time, as

$$\dot{M}_{\rm out} = \frac{V_{\rm out} M_{\rm out}}{R}. \quad (3)$$

We considered R as 500 pc. The distribution of $\dot{M}_{\rm out}$ for both the radio-detected and radio-undetected samples is illustrated in the middle right panel of Figure 2. According to the KS test, the distributions differ significantly, with a p-value of 5×10^{-5}. For the radio-detected sample, $\dot{M}_{\rm out}$ ranges from 2.3×10^{-4} to 5.1 $M_\odot\ \rm yr^{-1}$, with a mean of 0.17 $M_\odot\ \rm yr^{-1}$ and a median of 0.04 $M_\odot\ \rm yr^{-1}$ with median uncertainty of 0.004 $M_\odot\ \rm yr^{-1}$. For the radio-undetected sample, $\dot{M}_{\rm out}$ ranges from 8.0×10^{-5} to 0.2 $M_\odot\ \rm yr^{-1}$, with a mean of 0.03 $M_\odot\ \rm yr^{-1}$ and a median of 0.01 $M_\odot\ \rm yr^{-1}$ with median uncertainty of 0.002 $M_\odot\ \rm yr^{-1}$. These results indicate that $\dot{M}_{\rm out}$ is consistently higher in radio-detected sources than in radio-undetected ones.

4.2.7. Power of Outflows

The kinetic power of outflows ($\rm KP_{out}$) is defined as

$$\rm KP_{out} = \frac{1}{2}\dot{M}_{out} V_{out}^2. \quad (4)$$

The distribution of $\rm KP_{out}$ for our sample of sources is shown in the bottom left panel of Figure 2. The figure shows that radio-detected sources exhibit more powerful outflows than radio-undetected sources. From the KS test, we found that the distributions of $\rm KP_{out}$ for the radio-detected and radio-undetected samples are indeed different with a p-value of 2×10^{-7}.

For the radio-detected sample, $\rm KP_{out}$ ranges from 2.0×10^{37} to $1.8 \times 10^{42}\ \rm erg\ s^{-1}$, with a mean of $4.6 \times 10^{40}\ \rm erg\ s^{-1}$ and a median of $4.8 \times 10^{39}\ \rm erg\ s^{-1}$ with median uncertainty of $1.8 \times 10^{39}\ \rm erg\ s^{-1}$. In the radio-undetected sample, $\rm KP_{out}$ varies from 3.3×10^{37} to $7.0 \times 10^{40}\ \rm erg\ s^{-1}$, with a mean of $4.2 \times 10^{39}\ \rm erg\ s^{-1}$ and a median of $1.3 \times 10^{39}\ \rm erg\ s^{-1}$ with median uncertainty of $5.9 \times 10^{38}\ \rm erg\ s^{-1}$.

This indicates that radio-detected sources consistently exhibit higher outflow power than radio-undetected sources. This difference could suggest that radio emission is likely associated with more energetic outflows, possibly jets, potentially amplifying the impact of the AGN's feedback on the surrounding gas. Higher outflow power in radio-detected galaxies may be a sign of more efficient energy transfer from the AGN to the host galaxy's interstellar medium (ISM), possibly affecting star formation and the overall galactic environment (A. King & K. Pounds 2015).

4.2.8. Momentum Rate of Outflows

The momentum rate of outflows ($\dot{P}_{\rm out}$) is defined as $\dot{P}_{\rm out} = \dot{M}_{\rm out} V_{\rm out}$. The distribution of $\dot{P}_{\rm out}$ (outflow momentum rate) for the sample is shown in the bottom middle panel of Figure 2. According to the KS test, $\dot{P}_{\rm out}$ is significantly higher in radio-detected sources than in radio-undetected ones, with a p-value of 9×10^{-7}.

For radio-detected sources, $\dot{P}_{\rm out}$ spans from 8.3×10^{29} to $3.4 \times 10^{34}\ \rm g\ cm\ s^{-2}$, with a mean of $9.2 \times 10^{32}\ \rm g\ cm\ s^{-2}$ and a median of $1.7 \times 10^{32}\ \rm g\ cm\ s^{-2}$ with median uncertainty of $3.0 \times 10^{31}\ \rm g\ cm\ s^{-2}$. For the radio-undetected sources, $\dot{P}_{\rm out}$ ranges from 5.8×10^{29} to $1.2 \times 10^{33}\ \rm g\ cm\ s^{-2}$, with a mean of $1.1 \times 10^{32}\ \rm g\ cm\ s^{-2}$ and a median of $5.1 \times 10^{31}\ \rm g\ cm\ s^{-2}$ and with median uncertainty of $1.5 \times 10^{31}\ \rm g\ cm\ s^{-2}$. This indicates that $\dot{P}_{\rm out}$ is nearly an order of magnitude higher in radio-detected sources than in radio-undetected sources.

The elevated $\dot{P}_{\rm out}$ in radio-detected sources suggests a stronger coupling between the AGN energy and the outflow

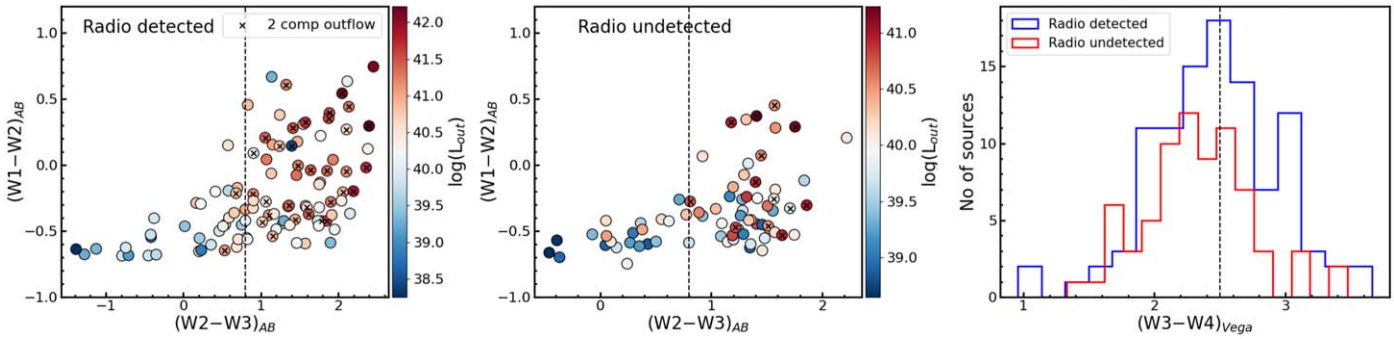

Figure 3. Infrared color–color diagram for the sources with outflows in the radio-detected sample (left panel) and radio-undetected sample (middle panel). Black crosses refer to sources with two outflow components. The color bar on the right indicates the total luminosity of the outflowing gas, and the vertical dashed line is the dividing line between AGN (left) and star-forming (right) according to J. Sabater et al. (2019). The right panel shows the distribution of W3 − W4 color. Here, too, the vertical line at W3 − W4 = 2.5 is the dividing line between AGN (to the left) and star-forming (to the right) sources (A. Caccianiga et al. 2015).

momentum, enhancing feedback effects on the host galaxy. Given the higher outflow power (KP_{out}) and mass outflow rates ($\dot{M}_{out}$) in these sources, it appears that radio activity is correlated with more efficient AGN feedback. This combination of higher momentum, power, and mass flow may drive larger-scale gas movements, which could potentially lead to the suppression or triggering of star formation in the host galaxy more effectively than in radio-undetected sources (A. C. Fabian 2012; A. King & K. Pounds 2015; C. Tadhunter 2016).

We have so far focused on the brightest outflowing component in this Section 4.2 when multiple components were detected. This approach may lead to an overrepresentation of highly ionized outflows while potentially underestimating those with higher velocities but lower ionization. To assess this potential bias, we conducted two additional analyses: one considering the less luminous outflows and another focusing on the outflows with higher velocities. The results of these analyses are provided in Appendix B (Tables B1, B2). Across all cases, we observed that radio-detected sources consistently exhibit higher velocities, mass outflow rates, outflow powers, and outflow momentum rates than their radio-undetected counterparts.

4.3. Outflows in Seyferts versus Liners

From Tables 2, B1, and B2, it is evident that $FWHM_{out}$ and V_{out} are significantly greater in LINERs than in Seyferts, suggesting higher outflow velocities in them. Additionally, a comparison of V_{shift} reveals that the outflows are more blueshifted in LINERs than in Seyferts. This larger velocity structure in LINERs may be linked to shock-dominated emission, as suggested by M. A. Dopita & R. S. Sutherland (1995). However, when considering the mass outflow rate, outflow power, and outflow momentum rate, Seyferts exhibit notably higher values, along with a greater outflow detection rate, as discussed in Section 4.1. This contrast is likely due to LINERs being at the low-luminosity end of AGN, with ionizing power and accretion rate lower than those of Seyferts (T. M. Heckman 1980; L. C. Ho 2008; I. Márquez et al. 2017), and producing less outflowing material, thereby resulting in lower detection rates and less powerful outflows.

4.4. Infrared Properties of Outflows

Of the sources analyzed in this work, more than half of them are found to show outflows, as evidenced by the presence of shifted broad asymmetric wings in their [O III] λ5007 line. Such an observed line profile could be the result of gas outflows from the central region of these sources (R. Zamanov et al. 2002). Such outflows can also be from the inner narrow-line region related to the winds from AGN (M. Elvis 2000). Alternatively, outflows can also be driven by star formation processes via winds from massive stars and/or Type 2 supernova explosions (E. Parlanti et al. 2024). Studies available in the literature point to infrared observations being an effective tool to distinguish between these two processes, namely AGN-driven and star formation-driven outflows. Therefore, to investigate the infrared properties of the sources with outflows, we cross-correlated our sources with the Wide-field Infrared Survey Explorer (WISE; E. L. Wright et al. 2010) catalog[5] using a search radius of 3″ for both our samples. To ensure reliable data for analysis, we only included sources with SNR greater than 3.0 in the W3 band. Since the WISE catalog provides magnitudes in the Vega system by default, we converted them to the AB magnitude system following the guidelines provided at https://wise2.ipac.caltech.edu/docs/release/allsky/expsup/sec4_4h.html.

We generated a color–color diagram using W2 − W3 and W1 − W2 in the AB system for both the radio-detected and radio-undetected samples, and this is depicted in the left and middle panels of Figure 3. Sources in this plot are classified into star formation and AGN, with a division at W2 − W3 = 0.8. According to this division (J. Sabater et al. 2019), sources to the left are AGN-dominated, and sources to the right are star formation-dominated. Thus, in our radio-detected and radio-undetected samples, a large fraction of sources with outflows lie in the region occupied by star-forming galaxies. Recently, N. Salem et al. (2024) found that sources with W2 − W3 < 0.16 in the AB system have very low specific star formation rate (sSFR) of $10^{-11.5}\,yr^{-1}$.

We also investigated the W3 − W4 color of our sample of sources with detected outflows, the distribution of which is shown in the right panel of Figure 3 in the Vega system. Here, too, sources with W3 − W4 < 2.5 are AGN-dominated, while sources with W3 − W4 > 2.5 are star formation-dominated (A. Caccianiga et al. 2015). The infrared color–color diagram and the W3 − W4 color indicate that a significant fraction of sources with detected outflows fall within the region typically associated with star-forming galaxies, despite all our sources being classified as AGN based on the BPT diagram. This suggests that infrared color is not a reliable metric for

[5] https://irsa.ipac.caltech.edu/Missions/wise.html

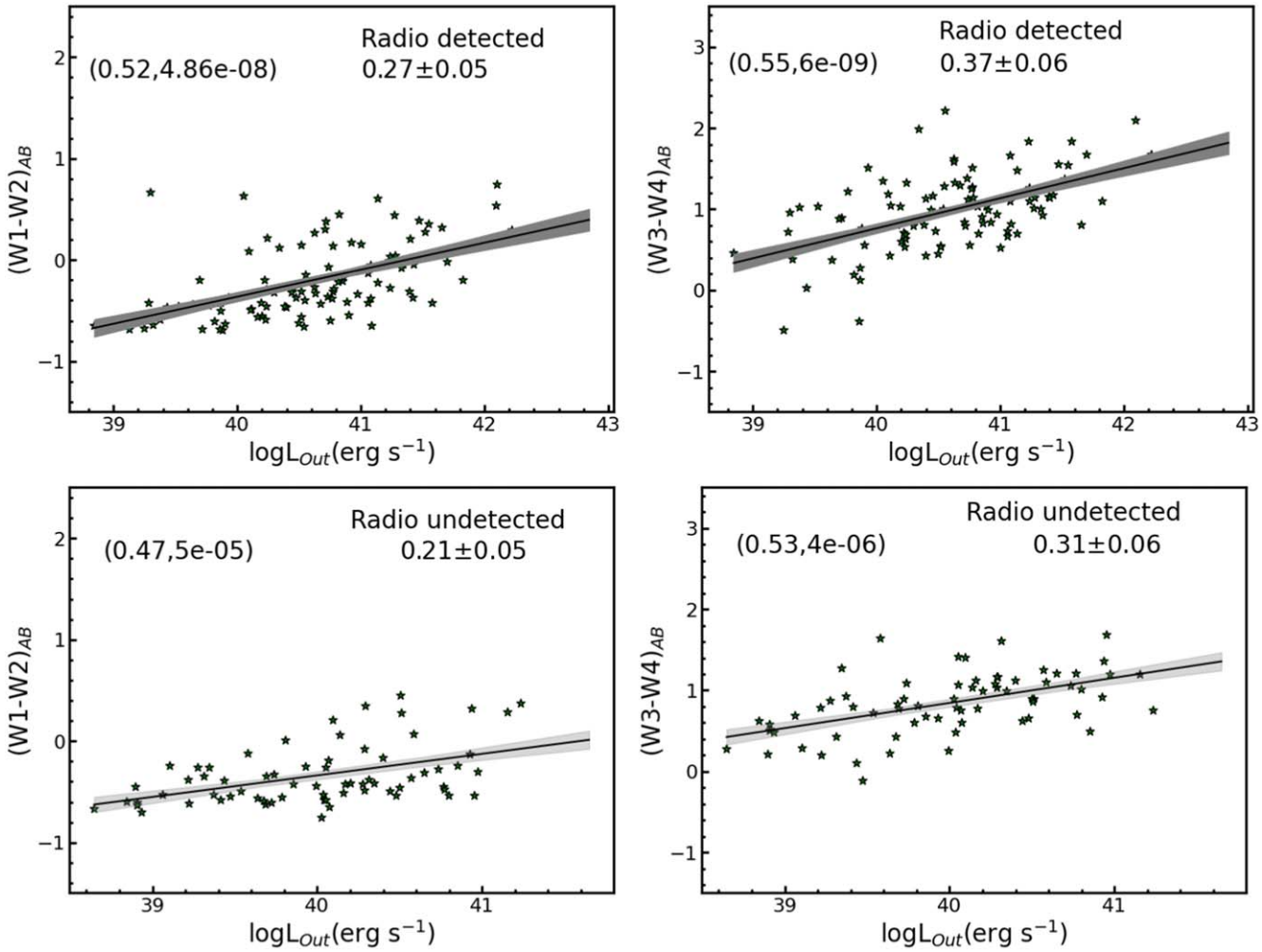

Figure 4. Variation of infrared colors with outflow luminosity for the radio-detected sample (upper panels) and for the radio-undetected sample (lower panels). The correlation coefficient and *p*-value from the KS test are displayed in the upper left corner of each plot, while the slope (see Section 4.8) is indicated in the upper right corner.

distinguishing between AGN-dominated and star formation-dominated sources.

Our analysis indicates that sources exhibiting outflows tend to have redder infrared (IR) colors, as illustrated in Figure 3. Additionally, we find a positive correlation between the IR colors W1 − W2 and W3 − W4 and the luminosity of the outflowing component (Figure 4) in both cases. Interestingly, the correlation is stronger for the W3 − W4 color than for W1 − W2. This pattern is consistent across both the radio-detected and radio-undetected samples. These correlations suggest that dust in the vicinity of the outflows is likely the dominant contributor to the observed mid-infrared (MIR) emission.

Furthermore, the AGN in our sample, classified based on their BPT diagnostics, display increased redness in outflowing sources (see Figures 3 and 4), which can be attributed to polar dust scattering. Dust grains absorb ultraviolet (UV) and optical radiation, reemitting it in the IR and thus producing the observed redder colors. This process not only affects the IR emission but also alters the ionization conditions of the surrounding gas, potentially influencing the chemical composition of the outflows and aiding the formation of various molecules (E. Järvelä et al. 2022).

Our results are in agreement with K. Zhang et al. (2013), who found that the MIR covering factor (the ratio of MIR luminosity to bolometric luminosity) correlates with the outflow component of [O III] λ5007, with the correlation strengthening at longer wavelengths. This was interpreted as evidence for IR emission produced by dust embedded within the outflows. Observations of several Seyfert galaxies also reveal that a significant fraction of their MIR emission originates along their polar directions, extending from a few parsecs to several hundred parsecs from the central engine. This emission is likely due to dust in the narrow-line region and/or dust driven by outflows (S. F. Hönig et al. 2013; M. Stalevski et al. 2019; H. Haidar et al. 2024).

4.5. Contribution of Star Formation to the Outflows

In the previous section, it was observed that the infrared properties of outflows reveal a redder color similar to that of star-forming galaxies. This raises the need to assess the contribution of star formation to the outflows in our sample of sources, where outflows were detected. Though the sources are classified as AGN according to the BPT diagrams, the influence of nuclear star formation could still be present in them. We aimed to assess the role of star formation in influencing outflows in the central 500×500 pc^2 region, which necessitates investigation of the star formation characteristics.

Numerous well-established tracers of star formation exist, such as strong emission lines in optical and infrared bands, as well as continuum emission from UV to radio wavelengths (R. C. Kennicutt & N. J. Evans 2012). However, these tracers are often contaminated by AGN emissions. Recently, A. Spindler et al. (2018) demonstrated that the sSFR derived from the strength of the Balmer 4000 Å break (D_n4000) is less impacted by AGN emission lines and thus can be a better diagnostic to constrain star formation (S. M. Wilkins et al. 2024). Consequently, we employed this method to examine the sSFR in our sample of sources.

We calculated D_n4000 by taking the ratio of the average of the flux density measurements in the red spectral range (4150–4250 Å) to the blue spectral range (3525–3625 Å). This is defined as

$$D_n4000 = \frac{\int_{4150}^{4250} f_\lambda d\lambda / \int_{4150}^{4250} d\lambda}{\int_{3525}^{3625} f_\lambda d\lambda / \int_{3525}^{3625} d\lambda}. \quad (5)$$

The chosen spectral window is slightly different from the one originally defined by A. G. Bruzual (1983), but it captures the break cleanly and does not cover the metal absorption lines (see also S. M. Wilkins et al. 2024 for the use of alternative wavelength windows). This wavelength window covers both the Balmer limit of 3645 Å, which is sensitive to young galaxies, and the 4000 Å break. The lower bound of the blue region for the break is determined by taking into account the instrument's shortest wavelength coverage that corresponds to the redshifted wavelengths of all observed sources.

The value of the D_n4000 parameter for our sample of radio-detected and radio-undetected sources ranges from 0.8 to 2.8. D_n4000 is close to unity for the galaxies dominated by O- and B-type stars (S. M. Wilkins et al. 2024), whereas D_n4000 is higher than 1.51 for a stellar population older than 1.1 Gyr (A. Paulino-Afonso et al. 2020).

A recent study by A. F. L. Bluck et al. (2020) on MaNGA sources found that regions of galaxies with D_n4000 larger than 1.45 are quenched with very low star formation, though the exact values of sSFR are not known but are less than $10^{-11.5}$ yr^{-1}. About 94% of the sources in the radio-detected sample and 99% of sources in the radio-undetected sample have D_n4000 larger than 1.45, which suggests substantially low or no star formation in this central region in our sample of sources. This may possibly be due to the negative feedback effect from AGN activity.

4.6. Origin of Outflows: AGN versus Star Formation

In Section 4.4, we observed that infrared diagnostics alone are insufficient to distinguish whether strong outflows originate from AGN activity or purely from star formation. However, in Section 4.5, using optical diagnostics such as the Balmer break, we found that in sources with outflows, the star formation is very low or negligible. By combining these two diagnostic methods and analyzing the position of the sources with outflows in the D_n4000 versus W3 − W4 plane, it would be possible to identify whether the detected outflows are due to star formation and/or AGN activity. We show in Figure 5 the plot of infrared color versus the Balmer break. From this figure, it is evident that most of our sources are situated in the AGN-dominated region. This new diagnostic diagram clearly indicates that the outflows found in sources with and without

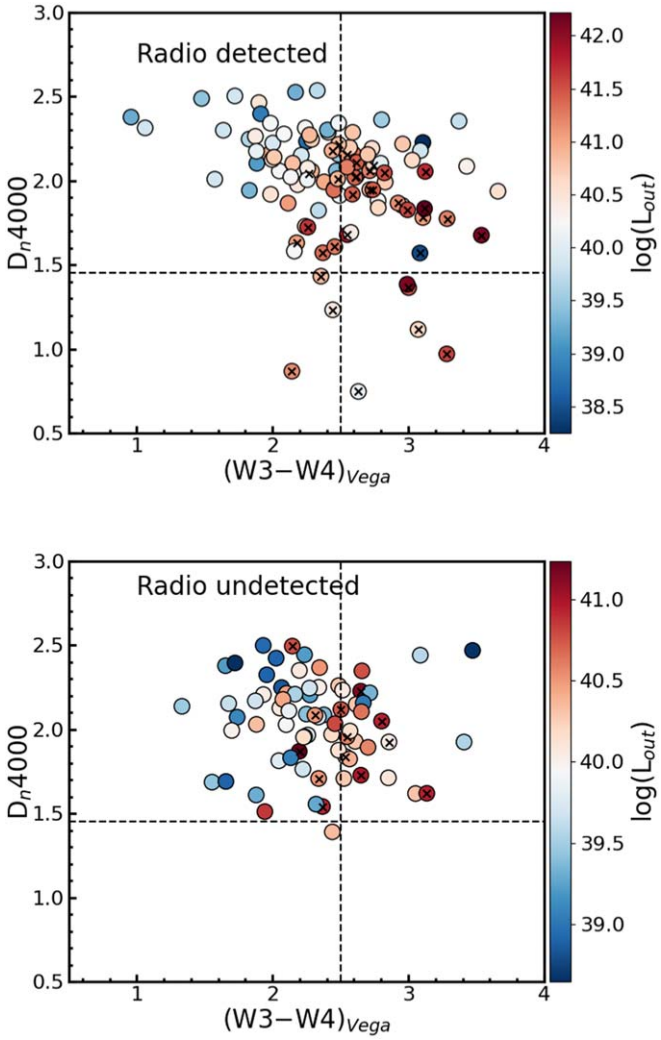

Figure 5. Position of the sources with outflows in the W3 − W4 vs. D_n4000 plane for radio-detected (upper panel) and radio-undetected (lower panel) samples. The color denotes the total luminosity of outflows. The black crosses are sources with two outflowing components. The vertical dashed line is $(W3 - W4)_{Vega} = 2.5$, the line separating pure star-forming sources and AGN. The horizontal line is for $D_n4000 = 1.45$.

radio emission are due to processes related to AGN. About 5% of the radio-detected sources with outflows lie in the region occupied by star formation with redder colors. In all these sources, both blueshifted (approaching component of outflows) and redshifted (receding component of outflows) components were detected. The redshifted component of the outflow, being located below the plane of the galaxy, is likely to be obscured by dust, and the observation that such sources are redder in color is not unexpected (S. Belli et al. 2024). Irrespective of that, contributions from both AGN and star formation to the observed outflows in this minority of sources could not be ruled out. Also, a large fraction of sources with $D_n4000 > 1.45$ (and thus negligible star formation) have redder colors, and this is likely due to the interaction of the outflowing gas with dust (E. Järvelä et al. 2022).

4.7. Cause of Radio Emission

From Section 4.6, it is clear that the observed outflows are due to AGN in both the samples of radio-detected and radio-undetected sources. Therefore, the observed radio emission in

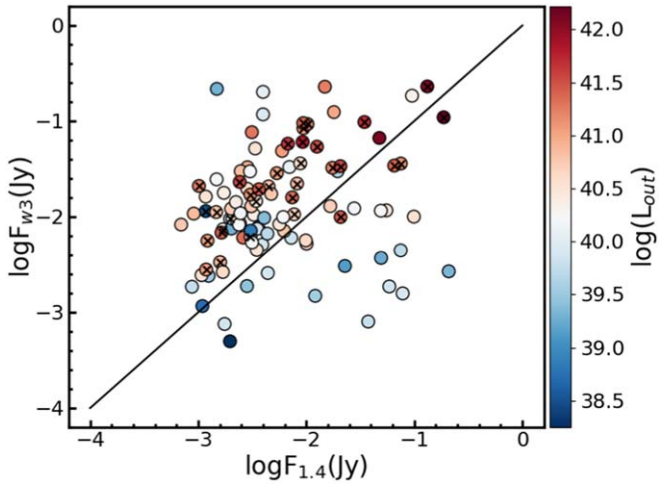

Figure 6. Location of the sources with outflows in the radio-detected sample in the F_{W3} vs. $F_{1.4\ GHz}$ plane. The solid black solid line is the $F_{W3} = F_{1.4\ GHz}$ line. The black crosses are sources with two components of outflows. The color denotes the luminosity of outflows.

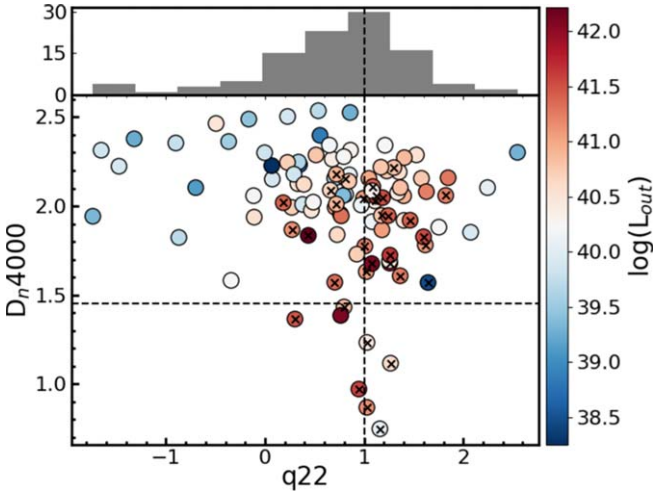

Figure 7. Position of outflow-detected sources in the radio-detected sample in the $q22$ vs. D_n4000 plane. The vertical line is $q22 = 1.0$, and the horizontal dashed line is $D_n4000 = 1.45$.

our radio-detected sample is unlikely to be due to star formation activities in their host galaxies, but rather attributed to processes related to AGN such as the presence of low-power radio jets, accretion disk coronas, as well as shocks due to outflows (F. Panessa et al. 2019; M. Liao et al. 2024). In this section, we aim to understand the origin of radio emission in our radio-detected sample, making use of diagnostic plots available in the literature. We show in Figure 6 the location of sources with outflows in the radio-detected sample in the F_{W3} versus $F_{1.4\ GHz}$ plane. For this plot, the radio flux density values were taken from the FIRST survey, while the flux density corresponding to the W3 band of WISE was taken from the WISE catalog. Also shown in the same plot is the $F_{W3} = F_{1.4\ GHz}$ line. According to D. Kozieł-Wierzbowska et al. (2021), sources below the line are radio AGN, while those above the line are starburst-dominated AGN. We also checked the $q22$ parameter defined as

$$q22 = \log(F_{22}/F_{1.4\ GHz}). \quad (6)$$

Here, F_{22} and $F_{1.4\ GHz}$ are the flux densities in the W4 band of the WISE and 1.4 GHz from FIRST respectively. The histogram of the $q22$ parameter is shown in Figure 7. Here, too, about 40% of the sources have $q22$ greater than unity, favoring star formation processes to be the cause of radio emission in them. In summary, although the $q22$ parameter and the F_{W3} versus $F_{1.4\ GHz}$ diagnostics indicate that in a large fraction of the sources the observed radio emission is likely to be associated with star formation activity, the plot of D_n4000 against $q22$ (Figure 7) shows that all sources bar six lie in the AGN-dominated region. This reddening could be due to dust scattering of AGN radiation. This reinforces the idea that the observed radio emission in our radio-detected sample is indeed AGN-dominated. High-resolution radio observations are the only direct way to identify which among the processes related to AGN are the cause of the observed radio emission in our sample. Though the detection of core jet structure is unambiguous evidence of a jet that produces the observed radio emission, the resolution of FIRST images used in this work is insufficient. In the absence of high-resolution observations, we assume in all further discussion that the observed radio emission is due to jet emission.

4.8. Correlation of Outflow Properties with Physical Properties of AGN

From various diagnostics, it is clear that the detected outflows are due to AGN. In this scenario, the driving force of outflows could be either from the radiation energy or the radio jets from AGN. To explore this, we analyzed the outflow properties alongside AGN properties such as M_{BH}, bolometric luminosity (L_{Bol}), and Eddington ratio (λ_{Edd}) for both the radio-detected and radio-undetected samples as well as the power of the radio jet (P_{Jet}) for the radio-detected sample. We determined M_{BH} adopting the dynamical method, using the M_{BH}–$\sigma_\star$ relation, where $\sigma_\star$ represents the stellar velocity dispersion. The $\sigma_\star$ values were obtained from the *Pipe3d* catalog (S. F. Sánchez et al. 2022) and are derived through stellar synthesis population modeling within one effective radius. Following the relation provided by D. Baron & B. Ménard (2019), which they validated for both Type 1 and Type 2 AGN, we calculated M_{BH} for all the sources in our sample.

We calculated L_{Bol} from Hα luminosity by following J. E. Greene & L. C. Ho (2005, 2007), wherein the luminosity of the Hα line was determined from the Hα flux taken from DAP and corrected for the effect of extinction. We also calculated λ_{Edd}, from Eddington luminosity L_{Edd}—the maximum luminosity emitted if the source is in hydrodynamical equilibrium—and L_{Bol}, as the ratio of L_{Bol} to L_{Edd}. L_{Edd} is defined as

$$L_{Edd} = 1.26 \times 10^{38}\left(\frac{M_{BH}}{M_\odot}\right) \text{erg s}^{-1}. \quad (7)$$

For the sample of radio-detected sources, we estimated P_{Jet} by following K. W. Cavagnolo et al. (2010) and considering that the radio emission from these sources is jet emission. For this, we used the 1.4 GHz luminosity ($L_{1.4}$) calculated using the integrated flux densities from the FIRST survey and corrected

Table 3
Results of the Fits to the Observed Data

Parameter	Radio-detected		Radio-undetected	
Y_{out} versus X_{AGN}	(R, p)	α	(R, p)	α
KP_{out} versus L_{Bol}	$(0.72, 7 \times 10^{-18})$	1.18 ± 0.14	$(0.52, 2 \times 10^{-6})$	0.81 ± 0.20
$\dot{M}_{out}$ versus L_{Bol}	$(0.74, 3 \times 10^{-19})$	1.07 ± 0.12	$(0.60, 9 \times 10^{-9})$	0.97 ± 0.17
KP_{out} versus P_{Jet}	$(0.36, 2 \times 10^{-4})$	0.56 ± 0.14	...	...
$\dot{M}_{out}$ versus P_{Jet}	(0.28, 0.004)	0.43 ± 0.12	...	...
KP_{out} versus P_{Jet} [$\log(L_{Bol}/P_{Jet}) > 0.4$]	$(0.64, 1 \times 10^{-11})$	0.99 ± 0.14	...	...
$\dot{M}_{out}$ versus P_{Jet} [$\log(L_{Bol}/P_{Jet}) > 0.4$]	$(0.58, 5 \times 10^{-9})$	0.79 ± 0.12	...	...

Note. Here, R and p are the correlation coefficient and probability for no correlation, respectively, for the Pearson correlation test. The quoted values of α, the power-law exponent, are the mean and one standard deviation (1σ).

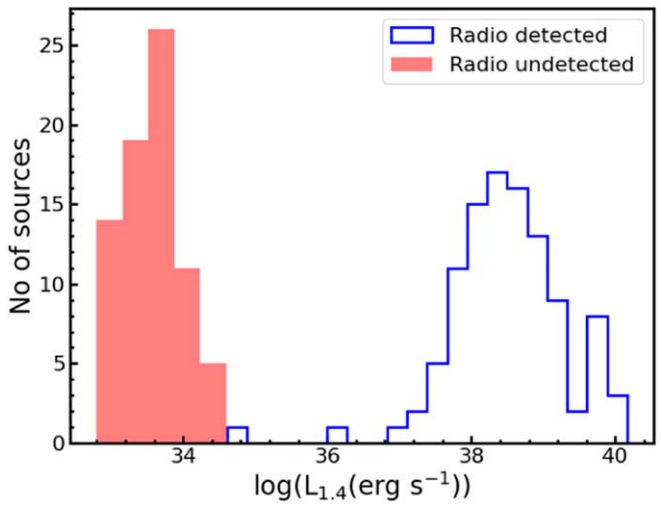

Figure 8. Distribution of $L_{1.4}$ for the radio-detected sample (blue). The shaded red region shows the upper limit of $L_{1.4}$ for the radio-undetected sample by considering the detection limit of the FIRST survey, which is 0.5 mJy.

for the effect of redshift assuming a spectral index ($S_\nu \propto \nu^{-\alpha}$) of 0.7 (J. J. Condon et al. 2002). The distribution of $L_{1.4}$ for our sample of radio-detected and radio-undetected sources is shown in Figure 8. For radio-undetected sources, the $L_{1.4}$ values are the upper limits that were calculated using the detection limit of the FIRST survey, which is 0.5 mJy.

After calculating these physical parameters of AGN, we compared them with outflow properties to explore potential correlations. In cases where two outflowing components were detected, we used the sum of the quantities deduced from the two components for the total outflow rate or the total kinetic power of outflows. We performed a statistical linear correlation test, the Pearson test, to identify significant correlations in terms of correlation coefficients and p-values. For parameters exhibiting significant correlations, we employed the Bayesian linear regression method using *LINMIX_ERR* (B. C. Kelly 2007) to fit a power-law relationship between the variables in log–log space. This method takes account of errors in both axes. If the AGN parameter is X_{AGN} and the outflow parameter is Y_{out} then the fitted function has the form

$$Y_{out} = A(X_{AGN})^{\alpha} \quad (8)$$

or

$$\log(Y_{out}) = \log A + \alpha \log(X_{AGN}) \quad (9)$$

where A is the multiplication constant and α is the power-law exponent. The best-fit values for α and the correlation coefficients for different parameters are summarized in Table 3.

From Table 3, it is evident that both $\dot{M}_{out}$ and KP_{out} are significantly correlated with L_{Bol} for both radio-detected and radio-undetected sources. This finding aligns with previous studies in the literature (F. Fiore et al. 2017; M. Bischetti et al. 2019; B. Musiimenta et al. 2023). While our results confirm the correlation between $\dot{M}_{out}$ and L_{Bol} noted in earlier works, we also emphasize the differences in the correlations between the two samples. Notably, the higher correlation coefficient and lower p-values for radio-detected sources suggest that this correlation is stronger in radio-detected sources than in their radio-undetected counterparts.

Examining the relationship of these outflow parameters with AGN luminosity, we found that for the radio-detected sample, we observed $\dot{M}_{out} \propto L_{Bol}^{1.07\pm0.12}$. In contrast, for the radio-undetected sample, $\dot{M}_{out} \propto L_{Bol}^{0.97\pm0.17}$. Though the slopes are consistent within 1σ, KP_{out} demonstrates a more pronounced difference: we found $KP_{out} \propto L_{Bol}^{1.18\pm0.14}$ for radio-detected sources, while for the radio-undetected sample we found $KP_{out} \propto L_{Bol}^{0.81\pm0.20}$. This indicates a steeper slope by 1σ for the radio-detected sources than for their undetected counterparts. This trend is illustrated in Figure 9, where we plot L_{Bol} against KP_{out} and $\dot{M}_{out}$, color-coded by λ_{Edd}. In the radio-detected category of sources, those with larger λ_{Edd} preferentially occupy the region with larger KP_{out}. This suggests a relationship between outflow power and λ_{Edd} for these sources. Conversely, this trend is not as clear for radio-undetected sources, as depicted on the right side of Figure 9.

The correlations observed in Figure 9 suggest multiple mechanisms are at play in driving outflows for radio-detected sources. While radiation from AGN is likely the primary driver of outflows in both radio-detected and radio-undetected sources, radio jets may serve as an additional mechanism that enhances outflow kinematics in radio-detected sources. This could explain the steeper correlation between KP_{out} and L_{Bol} in the radio-detected sample and the stronger correlation of KP_{out} with λ_{Edd}. Although there is a general upward trend of outflow properties with L_{Bol}, the scatter in the plots (see Figure 9) may be attributed to the complex interplay between outflows and the quantity or geometry of dense gas in the nuclear regions of these sources (C. Ramos Almeida et al. 2022). Moreover, the color coding in Figure 9 indicates that sources with high λ_{Edd} tend to have elevated values of L_{Bol}, $\dot{M}_{out}$, and KP_{out}. This

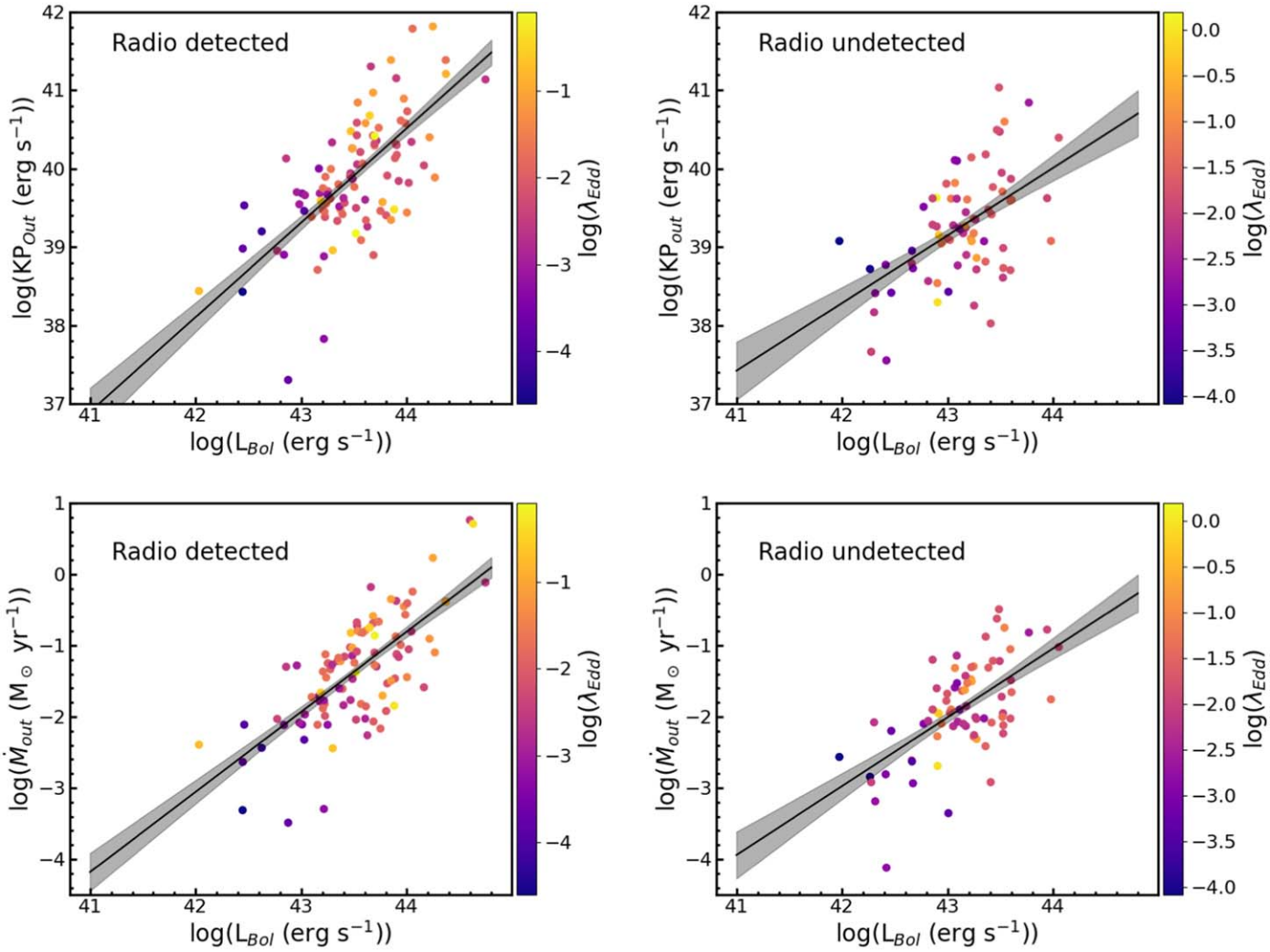

Figure 9. Upper panels: variation of total kinetic power of warm ionized outflow with $L_{\rm Bol}$ for radio-detected sources (left) and radio-undetected sources (right). Lower panels: variation of total outflow rate with $L_{\rm Bol}$ for the radio-detected sources (left) and radio-undetected sources (right). In each plot, the scatter points represent our data with 1σ error bars, while the solid line and shaded region indicate the fitted line with a 1σ confidence band. The color in each plot corresponds to $\lambda_{\rm Edd}$.

interpretation highlights the nuanced role of AGN radiation and radio jets in influencing outflow characteristics, suggesting a more complex feedback mechanism that merits further investigation.

For the radio-detected sample of sources, we found a flat relation between the outflow properties and jet power. We obtained the best-fit scaling relation $\mathrm{KP_{out}} \propto P_{\rm Jet}^{0.56\pm0.14}$ and $\dot{M}_{\rm out} \propto P_{\rm Jet}^{0.43\pm0.12}$. The results of the fits are given in Table 3. We also found the ratio $\log(L_{\rm Bol}/P_{\rm Jet})$ to have a bimodal behavior with a dividing limit at 0.4. We noticed that beyond this limit $P_{\rm Jet}$ is very strongly correlated with $L_{\rm Bol}$ with a slope of 0.96 ± 0.06, which can be seen in the upper panel of Figure 10. In the lower panel of Figure 10, we show the correlation between $\mathrm{KP_{out}}$ and $P_{\rm Jet}$. Here, the sources are color-coded with $\log(L_{\rm Bol}/P_{\rm Jet})$. We found that beyond the limit of $\log(L_{\rm Bol}/P_{\rm Jet}) = 0.4$, i.e., for $\log(L_{\rm Bol}/P_{\rm Jet}) > 0.4$, the correlation between $\mathrm{KP_{out}}$ and $P_{\rm Jet}$ is significantly strong and steep with$\mathrm{KP_{out}} \propto P_{\rm Jet}^{0.99\pm0.14}$. Below this limit, i.e., for higher $P_{\rm Jet}$ with similar $L_{\rm Bol}$, $\mathrm{KP_{out}}$ is lower. This may be due to the high-power jet encountering lower interaction with the cloud where [O III] λ5007 originates, reducing the outflow luminosity and leading to low outflow characteristics such as $\mathrm{KP_{out}}$ and $\dot{M}_{\rm out}$. Alternatively, a high-power jet can ionize the gas to its higher ionization state, leading to an outflow of low luminosity. Thus at any jet power, significant dominance of the jet power over bolometric luminosity can lead to weaker outflows.

This interpretation highlights the nuanced role of AGN radiation and radio jets in shaping outflow characteristics, suggesting a more complex feedback mechanism that warrants deeper exploration. Future studies can leverage high-resolution, multiwavelength observations to clarify the relative contributions of radiation-driven and jet-driven feedback processes. Spatially resolved spectroscopic studies, combined with detailed radio imaging, can help establish a clearer link between jet morphology and outflow kinematics. Additionally, theoretical modeling and simulations can provide further insights into the interplay between AGN-driven winds, jets, and the surrounding ISM. Investigating these aspects across a broader range of AGN types and host environments will be crucial for building a more comprehensive understanding of AGN feedback and its impact on galaxy evolution.

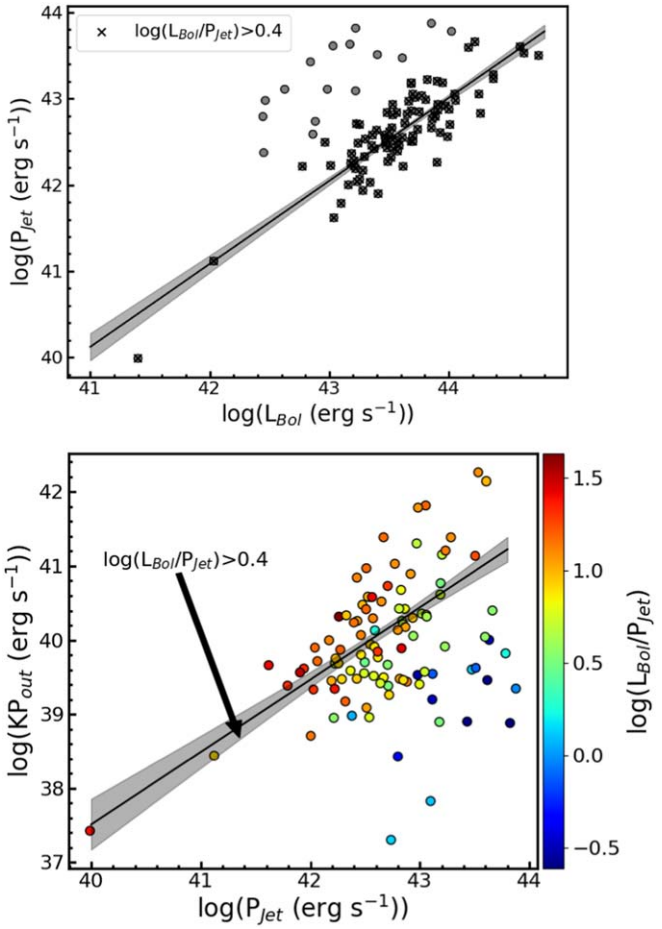

Figure 10. Upper panel: jet power vs. bolometric luminosity. The sources with $\log(L_{\rm Bol}/P_{\rm Jet}) > 0.4$ are shown with crosses. The fitted line is for the sources with $\log(L_{\rm Bol}/P_{\rm Jet}) > 0.4$. Lower panel: the variation of kinetic power of the outflow with jet power. The solid line with the shaded region is the fitted line with 1σ uncertainty for the given condition. The color in each plot corresponds to $L_{\rm Bol}/P_{\rm Jet}$ on the log scale.

5. Summary

In this study, we conducted a comparative analysis of outflow properties in radio-detected and radio-undetected sources in their central region of 500×500 pc^2. Our total sample consists of 538 AGN with a detected [O III] λ5007 line, mainly Seyfert and LINER types, of which 197 are radio-detected and 341 are radio-undetected. The objective was to identify outflows, study their properties, and constrain the role of AGN radiation and/or jets in driving outflows. For this, we used spatially resolved optical spectroscopic data from MaNGA and radio observations from FIRST surveys. We studied the properties of outflows and then compared them with AGN properties. Additionally, we explored the relationship between radio properties and outflow characteristics within the radio-detected sources. We summarize our main findings below.

1. To detect outflows, we carried out multiple Gaussian fits to the observed [O III] λ5007 line. In the radio-detected sample, $56\% \pm 7\%$ of sources showed evidence of outflows. However, in the radio-undetected sample, $25\% \pm 3\%$ of sources showed outflows. Thus, in our sample, the outflow detection rate is higher in radio-detected sources than in radio-undetected sources.
2. On separating our sample of sources into Seyferts and LINERs, outflows are detected more in Seyferts ($66\% \pm 7\%$) than LINERs ($15\% \pm 2\%$). This is true for both the radio-detected and radio-undetected samples. The mass outflow rate and outflow power are higher for Seyferts than LINERs, but the velocity structures are higher for LINERs than Seyferts.
3. In both the radio-detected and radio-undetected samples, for a majority of sources ($\sim$80%), we found the [O III] λ5007 line to have a blue asymmetry in addition to the narrow component. Also, in a minority of sources, we also observed the redshifted component in addition to the blueshifted component. The blueshifted component could be the approaching side of the outflow located above the plane of the galaxy, and the redshifted component could be the receding side of the outflow, located below the plane of the galaxy.
4. We observed distinct differences in the kinematics of the outflowing gas between the radio-detected and radio-undetected samples. The radio-detected sources exhibit higher velocity, larger velocity dispersion, greater asymmetry, larger outflow mass, and stronger kinematic power than the radio-undetected sources.
5. We found that in the infrared bands, more luminous outflows appear redder in color than weaker outflows. Infrared colors show a positive correlation with outflow luminosity, with this dependence becoming more pronounced in the mid-infrared band. This trend is primarily attributed to the presence of larger amounts of polar dust in the more powerful outflows.
6. We found a strong correlation between the outflow characteristics, such as $\dot{M}_{\rm out}$ and ${\rm KP}_{\rm out}$ of the outflow, and $L_{\rm Bol}$. Such a correlation points to radiation from AGN being the primary driver for outflows in both radio-detected and radio-undetected samples. However, this correlation between the outflow characteristics and the bolometric luminosity is mildly steeper for the radio-detected sample than for the radio-undetected sample. This suggests that in the radio-detected sample, radio jets could play an additional modest secondary role over and above the dominant role played by radiation in enhancing outflow kinematics.
7. Outflow characteristics are also found to show a correlation with $\lambda_{\rm Edd}$. Sources with higher $\lambda_{\rm Edd}$ appear to have higher $L_{\rm Bol}$, $M_{\rm out}$, and ${\rm KP}_{\rm out}$. This is true for both the radio-detected and radio-undetected samples.
8. For the radio-detected sample, we observed a bimodality in the distribution of log ($L_{\rm Bol}/P_{\rm Jet}$), with the dividing line at $\log(L_{\rm Bol}/P_{\rm Jet}) = 0.4$. In the correlation between the kinetic power of outflows and jet power, we found that at any jet power, significant dominance of the jet power over the bolometric luminosity can lead to weaker outflows.
9. We found the value of the D_n4000 parameter for our samples of radio-detected and radio-undetected sources to range between 0.8 and 2.8. About 94% of the sources in the radio-detected sample and 99% of sources in the radio-undetected sample have D_n4000 larger than 1.45, pointing to sSFR less than $10^{-11.5}\,{\rm yr}^{-1}$, which may possibly be due to negative AGN feedback.

Our findings suggest that ionized gas outflows, driven by the interaction between AGN radiation/winds and the ISM, are common across all AGN. However, the presence of radio jets appears to affect gas kinematics further, leading to a higher rate

of outflow detection in radio-detected sources, as evidenced by our study. Further investigations using high-resolution, multi-wavelength observations for different types of AGN may provide more insights toward understanding the feedback processes of radiation/winds and jets in greater detail. For example, high-resolution radio observations along with observations at other wavelengths would allow for a detailed spatial correlation between the morphology of radio jets and the outflowing gas, and understanding their kinematics.

Acknowledgments

We thank the reviewer for their comments and suggestions, which have helped to improve the manuscript. We also acknowledge Dr. Chris Harrison at Newcastle University for useful suggestions in the initial stage. This publication uses data from the MaNGA (Mapping Nearby Galaxies at APO) survey, which is one of the Sloan Digital Sky Survey (SDSS) IV programs. Funding for the Sloan Digital Sky Survey IV has been provided by the Alfred P. Sloan Foundation, the U.S. Department of Energy Office of Science, and the Participating Institutions.

SDSS-IV acknowledges support and resources from the Center for High Performance Computing at the University of Utah. The SDSS website is www.sdss4.org.

SDSS-IV is managed by the Astrophysical Research Consortium for the Participating Institutions of the SDSS Collaboration including the Brazilian Participation Group, the Carnegie Institution for Science, Carnegie Mellon University, Center for Astrophysics | Harvard & Smithsonian, the Chilean Participation Group, the French Participation Group, Instituto de Astrofisica de Canarias, The Johns Hopkins University, Kavli Institute for the Physics and Mathematics of the Universe (IPMU)/University of Tokyo, the Korean Participation Group, Lawrence Berkeley National Laboratory, Leibniz Institut für Astrophysik Potsdam (AIP), Max-Planck-Institut für Astronomie (MPIA Heidelberg), Max-Planck-Institut für Astrophysik (MPA Garching), Max-Planck-Institut für Extraterrestrische Physik (MPE), National Astronomical Observatories of China, New Mexico State University, New York University, University of Notre Dame, Observatário Nacional/MCTI, The Ohio State University, Pennsylvania State University, Shanghai Astronomical Observatory, United Kingdom Participation Group, Universidad Nacional Autónoma de México, University of Arizona, University of Colorado Boulder, University of Oxford, University of Portsmouth, University of Utah, University of Virginia, University of Washington, University of Wisconsin, Vanderbilt University, and Yale University. This project makes use of the MaNGA-Pipe3D data products. We thank the IA-UNAM MaNGA team for creating this catalog, and the Conacyt Project CB-285080 for supporting them

This publication uses radio observations carried out using the National Radio Astronomy Observatory facilities VLA of FIRST survey. The National Radio Astronomy Observatory is a facility of the National Science Foundation operated under a cooperative agreement by Associated Universities, Inc. This work has made use of the NASA Astrophysics Data System (ADS)[6] and the NASA/IPAC extragalactic database (NED).[7] P.N. thanks the Council of Scientific and Industrial Research (CSIR), Government of India, for supporting the research under the CSIR Junior/Senior research fellowship program through the grant No. 09/079(2867)/2021 − *EMR* − *I*.

Facilities: Sloan, VLA.

Software: Topcat (M. B. Taylor 2005), Numpy (C. R. Harris et al. 2020), Astropy (Astropy Collaboration et al. 2022), Scipy (P. Virtanen et al. 2020), Matplotlib (J. D. Hunter 2007), PyNeb (V. Luridiana et al. 2015), LINMIX_ERR (B. C. Kelly 2007).

Appendix A
Sample and Emission-line Fits

As described in Section 2, our sample to study the mechanisms that trigger warm ionized outflows in AGN is from

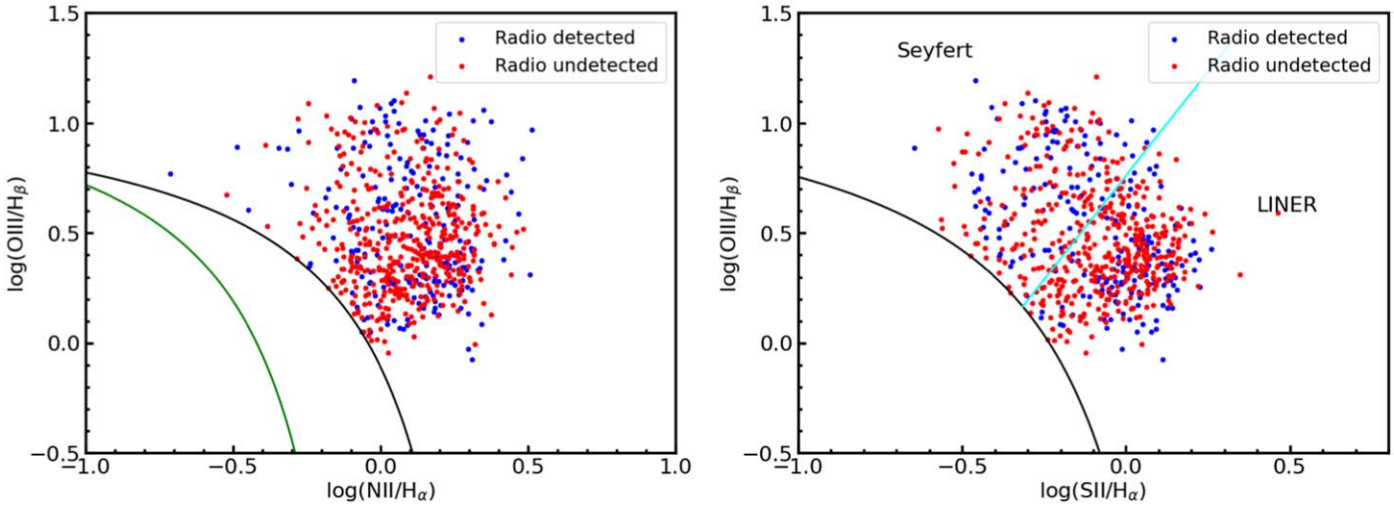

Figure A1. Positions of the sources in the [N II]/Hα BPT diagram (left) and [S II]/Hα BPT diagram (right). The black and green solid lines separate the region occupied by AGN and star-forming galaxies according to L. J. Kewley et al. (2001) and G. Kauffmann et al. (2003), respectively. The cyan solid line separates Seyfert galaxies and LINERs (L. J. Kewley et al. 2001). Filled blue and red circles refer to radio-detected and radio-undetected sources.

[6] https://ui.adsabs.harvard.edu/
[7] https://ned.ipac.caltech.edu

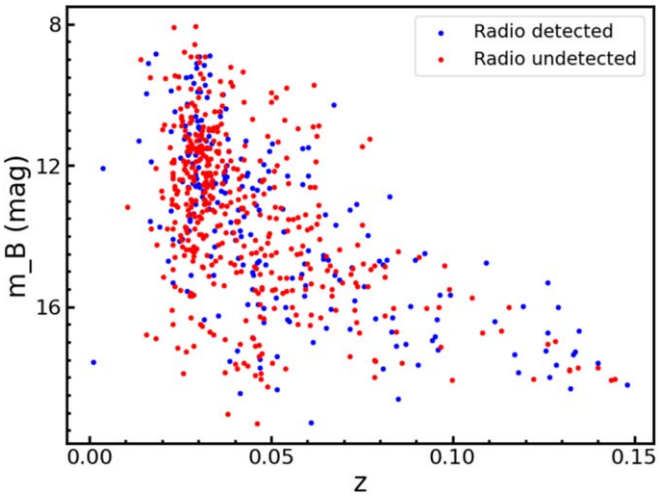

Figure A2. Distribution of sources in the plane of redshift vs. *B*-band apparent magnitude. Here, the filled blue and red circles refer to the radio-detected and radio-undetected sources, respectively.

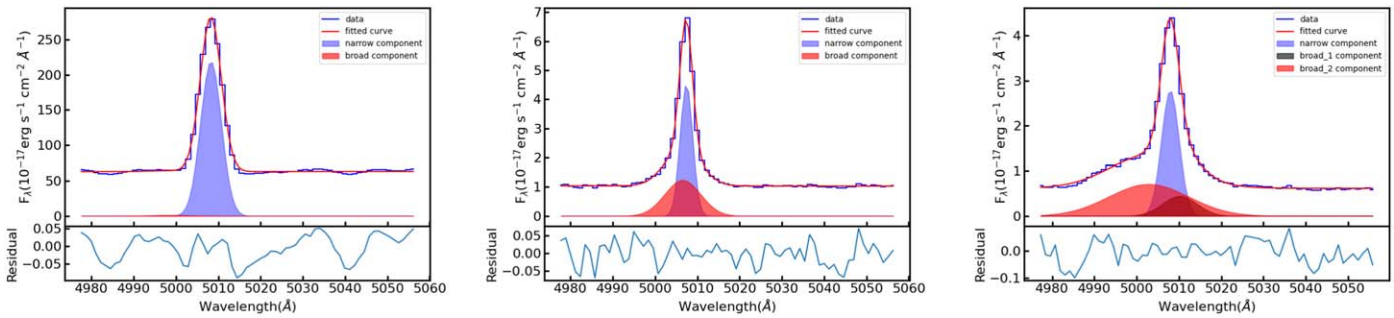

Figure A3. Example line fits to the [O III] λ5007 line for an outflow-undetected source (left panel) and an outflow-detected source (middle and right panels). A single Gaussian profile nicely describes the observed line profile (left panel), while two and three Gaussian components (two phases of outflow) were required for the observed line profiles in the middle and right panels. The broad Gaussian components in the middle and right panels show the presence of an outflow.

MaNGa, which contains both AGN and non-AGN sources. We therefore selected the AGN sources by constructing BPT diagrams. The positions of the sources in the final sample in the BPT diagrams are shown in Figure A1. The AGN sources thus selected were divided into radio-detected and radio-undetected ones.

The distribution of the sources in the plane of redshift versus optical *B*-band brightness is shown in Figure A2.

To identify warm ionized outflows in the final sample of AGN, we carried out Gaussian fits to the [O III] λ5007 line. Sample fits are shown in Figure A3.

Appendix B
Kinematic Properties of the Less Luminous and High-speed Outflows

To investigate the kinematic properties of the outflows in both the radio-detected and radio-undetected samples (Section 4.2), we have initially used the brightest components, the results for which are given in Table 2. We also carried out a similar analysis using the less luminous outflows and the higher-velocity outflows, the results of which are given in Tables B1 and B2 respectively.

Table B1
Kinematic Properties of the Less Luminous Outflows

(a) Radio-detected

Parameter	Total			Seyferts			LINERs		
	Range	Mean	Median	Range	Mean	Median	Range	Mean	Median
V_{shift} (km s^{-1})	−695.0 to 882.0	−194.0	−198.0	−583.0 to 882.0	−127.0	−163.0	−695.0 to 258.0	−376.0	−449.0
FWHM$_{out}$ (km s^{-1})	156.0–1401.0	653.0	635.0	156.0–1401.0	644.0	619.0	257.0–1018.0	678.0	737.0
V_{out} (km s^{-1})	308.0–1503.0	823.0	818.0	308.0–1503.0	768.0	733.0	378.0–1400.0	973.0	1084.0
AI	−0.46 to 0.12	−0.15	−0.16	−0.34 to 0.12	−0.14	−0.15	−0.46 to 0.11	−0.18	−0.16
M_{out} (10^2 $M_\odot$)	1.11–23,558.28	775.31	235.03	1.11–23,558.28	960.12	348.17	1.81–2120.98	273.7	41.16
$\dot{M}_{out}$ (10^{-3} $M_\odot$ yr^{-1})	0.07–5112.32	145.64	33.95	0.07–5112.32	183.5	43.07	0.33–424.39	42.87	8.02
KP$_{out}$ (10^{38} erg s^{-1})	0.02–18,166.25	489.61	47.73	0.02–18,166.25	629.0	62.1	0.2–697.58	124.27	57.6
$\dot{P}_{out}$ (10^{30} g cm s^{-2})	0.14–34,222.09	922.0	134.0	0.14–34,222.09	1175.24	181.62	0.91–2761.69	234.64	60.19

(b) Radio-undetected

Parameter	Total			Seyferts			LINERs		
	Range	Mean	Median	Range	Mean	Median	Range	Mean	Median
V_{shift} (km s^{-1})	−657.0 to 227.0	−277.0	−235.0	−657.0 to 227.0	−225.0	−186.0	−624.0 to −211.0	−526.0	−585.0
FWHM$_{out}$ (km s^{-1})	152.0–1171.0	560.0	577.0	152.0–1151.0	527.0	505.0	580.0–1171.0	720.0	672.0
V_{out} (km s^{-1})	237.0–1387.0	769.0	733.0	237.0–1343.0	692.0	643.0	849.0–1387.0	1137.0	1136.0
AI	−0.51 to 0.16	−0.18	−0.17	−0.51 to 0.16	−0.15	−0.13	−0.44 to −0.01	−0.33	−0.37
M_{out} (10^2 $M_\odot$)	0.3–1481.81	202.86	78.37	4.7–1481.81	228.63	91.57	0.3–616.59	79.95	33.35
$\dot{M}_{out}$ (10^{-3} $M_\odot$ yr^{-1})	0.08–247.09	24.88	9.87	1.08–247.09	26.1	11.58	0.08–151.93	19.11	7.42
KP$_{out}$ (10^{38} erg s^{-1})	0.36–1053.8	59.27	14.97	0.46–1053.8	54.11	14.42	0.36–696.0	83.9	22.41
$\dot{P}_{out}$ (10^{30} g cm s^{-2})	0.58–1812.07	123.71	52.05	2.63–1812.07	119.91	55.32	0.58–1154.74	141.85	50.95

Table B2
Kinematic Properties of the High-speed Outflows

(a) Radio-detected

Parameter	Total			Seyferts			LINERs		
	Range	Mean	Median	Range	Mean	Median	Range	Mean	Median
V_{shift} (km s^{-1})	−782.0 to 882.0	−198.0	−193.0	−782.0 to 882.0	−133.0	−133.0	−695.0 to 258.0	−376.0	−449.0
FWHM$_{out}$ (km s^{-1})	176.0–1401.0	728.0	682.0	176.0–1401.0	731.0	679.0	257.0–1018.0	678.0	737.0
V_{out} (km s^{-1})	337.0–1970.0	879.0	864.0	337.0–1970.0	844.0	826.0	378.0–1400.0	973.0	1084.0
AI	−0.46 to 0.12	−0.15	−0.16	−0.34 to 0.12	−0.14	−0.15	−0.46 to 0.11	−0.18	−0.16
M_{out} (10^2 $M_\odot$)	1.81–23,558.28	831.92	239.35	1.89–23,558.28	1037.58	384.92	1.81–2120.98	273.7	41.16
$\dot{M}_{out}$ (10^{-3} $M_\odot$ yr^{-1})	0.23–5112.32	163.81	42.14	0.23–5112.32	208.36	56.62	0.33–424.39	42.87	8.02
KP$_{out}$ (10^{38} erg s^{-1})	0.2–18,166.25	602.86	62.1	0.24–18,166.25	783.98	101.5	0.2–1425.12	111.26	34.4
$\dot{P}_{out}$ (10^{30} g cm s^{-2})	0.83–34,222.09	1079.06	180.65	0.83–34,222.09	1390.16	267.04	0.91–2761.69	234.64	60.19

(b) Radio-undetected

Parameter	Total			Seyferts			LINERs		
	Range	Mean	Median	Range	Mean	Median	Range	Mean	Median
V_{shift} (km s^{-1})	−657.0 to 177.0	−278.0	−235.0	−657.0 to 177.0	−225.0	−185.0	−624.0 to −211.0	−526.0	−585.0
FWHM$_{out}$ (km s^{-1})	172.0–1171.0	575.0	580.0	172.0–1151.0	545.0	536.0	580.0–1171.0	720.0	672.0
V_{out} (km s^{-1})	312.0–1387.0	777.0	733.0	312.0–1343.0	701.0	657.0	849.0–1387.0	1137.0	1136.0
AI	−0.51 to 0.16	−0.18	−0.17	−0.51 to 0.16	−0.15	−0.13	−0.44 to −0.01	−0.33	−0.37
M_{out} (10^2 $M_\odot$)	0.3–1488.25	207.14	84.41	4.7–1488.25	233.8	94.93	0.3–616.59	79.95	33.35
$\dot{M}_{out}$ (10^{-3} $M_\odot$ yr^{-1})	0.08–247.09	26.72	9.97	1.08–247.09	28.32	11.58	0.08–151.93	19.11	7.42
KP$_{out}$ (10^{38} erg s^{-1})	0.36–1053.8	63.07	14.99	0.46–1053.8	58.71	14.98	0.36–696.0	83.9	22.41
$\dot{P}_{out}$ (10^{30} g cm s^{-2})	0.58–1812.07	133.73	52.05	2.63–1812.07	132.02	55.32	0.58–1154.74	141.85	50.95

ORCID iDs

Payel Nandi https://orcid.org/0009-0003-9765-3517
C. S. Stalin https://orcid.org/0000-0002-4998-1861
D. J. Saikia https://orcid.org/0000-0002-4464-8023

References

Aalto, S., Costagliola, F., Muller, S., et al. 2016, A&A, 590, A73
Astropy Collaboration, Price-Whelan, A. M., Lim, P. L., et al. 2022, ApJ, 935, 167
Audibert, A., Ramos Almeida, C., García-Burillo, S., et al. 2023, A&A, 671, L12
Ayubinia, A., Woo, J.-H., Rakshit, S., & Son, D. 2023, ApJ, 954, 27
Baldwin, J. A., Phillips, M. M., & Terlevich, R. 1981, PASP, 93, 5
Baron, D., & Ménard, B. 2019, MNRAS, 487, 3404
Becker, R. H., White, R. L., & Helfand, D. J. 1995, ApJ, 450, 559
Belli, S., Park, M., Davies, R. L., et al. 2024, Natur, 630, 54
Bischetti, M., Piconcelli, E., Feruglio, C., et al. 2019, A&A, 628, A118
Bluck, A. F. L., Maiolino, R., Sánchez, S. F., et al. 2020, MNRAS, 492, 96
Bruzual, A. G. 1983, ApJ, 273, 105
Bundy, K., Bershady, M. A., Law, D. R., et al. 2015, ApJ, 798, 7
Caccianiga, A., Antón, S., Ballo, L., et al. 2015, MNRAS, 451, 1795
Calzetti, D., Armus, L., Bohlin, R. C., et al. 2000, ApJ, 533, 682
Cardelli, J. A., Clayton, G. C., & Mathis, J. S. 1989, ApJ, 345, 245
Carniani, S., Venturi, G., Parlanti, E., et al. 2024, A&A, 685, A99
Cattaneo, A., & Best, P. N. 2009, MNRAS, 395, 518
Cavagnolo, K. W., McNamara, B. R., Nulsen, P. E. J., et al. 2010, ApJ, 720, 1066
Condon, J. J., Cotton, W. D., & Broderick, J. J. 2002, AJ, 124, 675
do Nascimento, J. C., Dors, O. L., Storchi-Bergmann, T., et al. 2022, MNRAS, 513, 807
Dopita, M. A., & Sutherland, R. S. 1995, ApJ, 455, 468
Elvis, M. 2000, ApJ, 545, 63
Fabian, A. C. 2012, ARA&A, 50, 455
Fernández-Ontiveros, J. A., Dasyra, K. M., Hatziminaoglou, E., et al. 2020, A&A, 633, A127
Feruglio, C., Fiore, F., Carniani, S., et al. 2015, A&A, 583, A99
Fiore, F., Feruglio, C., Shankar, F., et al. 2017, A&A, 601, A143
Flesch, E. W. 2023, OJAp, 6, 49
García-Burillo, S., Combes, F., Usero, A., et al. 2014, A&A, 567, A125
Girdhar, A., Harrison, C. M., Mainieri, V., et al. 2022, MNRAS, 512, 1608
Greene, J. E., & Ho, L. C. 2005, ApJ, 630, 122
Greene, J. E., & Ho, L. C. 2007, ApJ, 670, 92
Guo, Y., Bacon, R., Bouché, N. F., et al. 2023, Natur, 624, 53
Haidar, H., Rosario, D. J., Alonso-Herrero, A., et al. 2024, MNRAS, 532, 4645
Harris, C. R., Millman, K. J., van der Walt, S. J., et al. 2020, Natur, 585, 357
Harrison, C. M., Alexander, D. M., Mullaney, J. R., & Swinbank, A. M. 2014, MNRAS, 441, 3306
Heckman, T. M. 1980, A&A, 87, 152
Ho, L. C. 2008, ARA&A, 46, 475
Hönig, S. F., Kishimoto, M., Tristram, K. R. W., et al. 2013, ApJ, 771, 87
Hunter, J. D. 2007, CSE, 9, 90
Husemann, B., Bennert, V. N., Jahnke, K., et al. 2019, ApJ, 879, 75
Izumi, T., Wada, K., Imanishi, M., et al. 2023, Sci, 382, 554
Järvelä, E., Dahale, R., Crepaldi, L., et al. 2022, A&A, 658, A12
Jarvis, M. E., Harrison, C. M., Thomson, A. P., et al. 2019, MNRAS, 485, 2710
Kauffmann, G., Heckman, T. M., Tremonti, C., et al. 2003, MNRAS, 346, 1055
Kelly, B. C. 2007, ApJ, 665, 1489
Kennicutt, R. C., & Evans, N. J. 2012, ARA&A, 50, 531
Kewley, L. J., Heisler, C. A., Dopita, M. A., & Lumsden, S. 2001, ApJS, 132, 37
King, A., & Pounds, K. 2015, ARA&A, 53, 115
Kozieł-Wierzbowska, D., Vale Asari, N., Stasińska, G., et al. 2021, ApJ, 910, 64
Kukreti, P., Morganti, R., Tadhunter, C., & Santoro, F. 2023, A&A, 674, A198
Law, D. R., Belfiore, F., Bershady, M. A., et al. 2022, ApJ, 928, 58
Law, D. R., Cherinka, B., Yan, R., et al. 2016, AJ, 152, 83
Liao, M., Wang, J., Ren, W., & Zhou, M. 2024, MNRAS, 528, 3696
Luridiana, V., Morisset, C., & Shaw, R. A. 2015, A&A, 573, A42
Lynden-Bell, D. 1969, Natur, 223, 690
Márquez, I., Masegosa, J., González-Martin, O., et al. 2017, FrASS, 4, 34
Martín-Navarro, I., Brodie, J. P., Romanowsky, A. J., Ruiz-Lara, T., & van de Ven, G. 2018, Natur, 553, 307
Miller, J. S., & Mathews, W. G. 1972, ApJ, 172, 593
Molyneux, S. J., Harrison, C. M., & Jarvis, M. E. 2019, A&A, 631, A132
Morganti, R., Oosterloo, T., Oonk, J. B. R., Frieswijk, W., & Tadhunter, C. 2015, A&A, 580, A1
Mullaney, J. R., Alexander, D. M., Fine, S., et al. 2013, MNRAS, 433, 622
Murthy, S., Morganti, R., Wagner, A. Y., et al. 2022, NatAs, 6, 488
Musiimenta, B., Brusa, M., Liu, T., et al. 2023, A&A, 679, A84
Nandi, P., Stalin, C. S., Dam, P., & Saikia, D. J. 2024, ApJ, 973, 7
Nandi, P., Stalin, C. S., Saikia, D. J., et al. 2023a, ApJ, 950, 81
Nandi, P., Stalin, C. S., Saikia, D. J., et al. 2023b, ApJ, 959, 116
Osterbrock, D. E., & Ferland, G. J. 2006, Astrophysics of Gaseous Nebulae and Active Galactic Nuclei (2; Sausalito, CA: Univ. Science Books)
Padovani, P. 2017, NatAs, 1, 0194
Padovani, P., Alexander, D. M., Assef, R. J., et al. 2017, A&ARv, 25, 2
Panessa, F., Baldi, R. D., Laor, A., et al. 2019, NatAs, 3, 387
Parlanti, E., Carniani, S., Venturi, G., et al. 2025, A&A, 695, A6
Paulino-Afonso, A., Sobral, D., Darvish, B., et al. 2020, A&A, 633, A70
Ramos Almeida, C., Bischetti, M., García-Burillo, S., et al. 2022, A&A, 658, A155
Reines, A. E. 2022, NatAs, 6, 26
Riffel, R. A., Storchi-Bergmann, T., Riffel, R., et al. 2023, MNRAS, 521, 1832
Sabater, J., Best, P. N., Hardcastle, M. J., et al. 2019, A&A, 622, A17
Saikia, D. J. 2022, JApA, 43, 97
Salem, N., Masters, K. L., Stark, D. V., & Sharma, A. 2024, RNAAS, 8, 188
Sánchez, S. F., Barrera-Ballesteros, J. K., Lacerda, E., et al. 2022, ApJS, 262, 36
Speranza, G., Ramos Almeida, C., Acosta-Pulido, J. A., et al. 2022, A&A, 665, A55
Spindler, A., Wake, D., Belfiore, F., et al. 2018, MNRAS, 476, 580
Stalevski, M., Tristram, K. R. W., & Asmus, D. 2019, MNRAS, 484, 3334
Su, R., Mahony, E. K., Gu, M., et al. 2023, MNRAS, 520, 5712
Tadhunter, C. 2016, A&ARv, 24, 10
Taylor, M. B. 2005, in ASP Conf. Ser. 347, Astronomical Data Analysis Software and Systems XIV, ed. P. Shopbell, M. Britton, & R. Ebert (San Francisco, CA: ASP), 29
Torres-Papaqui, J. P., Coziol, R., Robleto-Orús, A. C., Cutiva-Alvarez, K. A., & Roco-Avilez, P. 2024, AJ, 168, 37
Veilleux, S., Kim, D. C., Sanders, D. B., Mazzarella, J. M., & Soifer, B. T. 1995, ApJS, 98, 171
Venturi, G., Cresci, G., Marconi, A., et al. 2021, A&A, 648, A17
Venturi, G., Treister, E., Finlez, C., et al. 2023, A&A, 678, A127
Virtanen, P., Gommers, R., Oliphant, T. E., et al. 2020, NatMe, 17, 261
Wake, D. A., Bundy, K., Diamond-Stanic, A. M., et al. 2017, AJ, 154, 86
Westfall, K. B., Cappellari, M., Bershady, M. A., et al. 2019, AJ, 158, 231
Wilkins, S. M., Lovell, C. C., Irodotou, D., et al. 2024, MNRAS, 527, 7965
Woo, J.-H., Bae, H.-J., Son, D., & Karouzos, M. 2016, ApJ, 817, 108
Wright, E. L., Eisenhardt, P. R. M., Mainzer, A. K., et al. 2010, AJ, 140, 1868
Wylezalek, D., & Morganti, R. 2018, NatAs, 2, 181
Zakamska, N. L., & Greene, J. E. 2014, MNRAS, 442, 784
Zamanov, R., Marziani, P., Sulentic, J. W., et al. 2002, ApJL, 576, L9
Zhang, K., Wang, T.-G., Yan, L., & Dong, X.-B. 2013, ApJ, 768, 22
Zhuang, M.-Y., & Ho, L. C. 2023, NatAs, 7, 1376